

The Effect of Biofilms on Turbulent Flow over Permeable Beds

Farzan Kazemifar¹, Gianluca Blois², Marcelo Aybar^{3*}, Patricia Perez Calleja³, Robert Nerenberg³, Sumit Sinha^{4‡}, Richard J. Hardy⁴, Jim Best⁵, Gregory H. Sambrook Smith⁶, Kenneth T. Christensen^{2,3,7}

¹Department of Mechanical Engineering, San Jose State University, USA. ²Department of Aerospace and Mechanical Engineering, University of Notre Dame, USA. ³Department of Civil and Environmental Engineering and Earth Sciences, University of Notre Dame, USA. ⁴Department of Geography, Durham University, UK. ⁵Departments of Geology, Geography and GIS, and Mechanical Science and Engineering and Ven Te Chow Hydrosystems Laboratory, University of Illinois at Urbana-Champaign, USA. ⁶School of Geography, Earth and Environmental Sciences, University of Birmingham, UK. ⁷International Institute for Carbon Neutral Energy Research (I²CNER), Kyushu University, Japan.

Corresponding author: Kenneth Christensen (christensen.33@nd.edu)

* Current address: Department of Civil Engineering, Universidad de Concepción, Chile.

‡ Current address: School of Earth and Environment, University of Leeds, UK.

Key Points:

- The effect of presence of biofilm on turbulence in the free flow is due to a combination of reduced bed porosity and change in geometry and roughness.
- Presence of biofilm increases Reynolds stresses in the outer layer scaling with wall shear stress.
- Presence of biofilm dampens dimensionless Reynolds stresses in the vicinity of the permeable bed.

Abstract

Despite an increasingly large body of work advancing our understanding of flow interactions occurring at the interface of a turbulent flow overlying a permeable bed, little is known concerning how such flow may be affected by the presence of biofilms, which exist in nearly all aquatic environments. This paper quantifies the effects on flow exerted by biofilms grown over experimental laboratory permeable beds until biofilm detachment, and then compares this to the residual effects after its detachment. The investigation is conducted in a flow channel by immersing two-dimensional permeable beds with idealized geometry and different porosities in order to explore different bed permeabilities. Sequences of increasingly higher flow velocity conditions followed by lower flow, were considered to explore the effect of detachment. Measurements were performed using particle image velocimetry. The total wall shear stress and friction velocity were found to increase in the presence of pre-grown biofilm, and decrease after biofilm detachment, when compared at the same pump frequency. The dimensionless Reynolds stresses, at constant pump frequency, collapsed for different bed configurations in the outer layer, while for the inner layer, the presence of biofilm led to a decrease in dimensionless Reynolds stress. Quadrant analysis shows that this decrease was primarily due to a reduction in strong Q2 contributions. These results suggest that models for flow and transport over permeable media in aquatic environments cannot neglect the role of biofilms in modifying turbulence.

1 Introduction

Flows over porous media are central to key biogeochemical processes occurring in many natural and industrial aquatic systems. In particular, exchange of mass, momentum, nutrients and heat in the hyporheic zone is central to many hydrologic systems (Cardenas 2015; Packman and Bencala 2000; Sternecker, Wild, and Geist 2013). For example, in alluvial channels recent studies have shown that bed porosity results in the generation of a diverse mosaic of turbulent suction and ejection events that are fundamentally different from those occurring over impermeable walls (Blois et al. 2011, 2014; Kim et al. 2018; Manes, Pokrajac, et al. 2011; Sinha et al. 2017; Stoesser and Rodi 2007; Suga et al. 2010). Knowledge of these dynamics, at a range of scales, is important due to their critical role in sedimentation, as well as transport of nutrients, pollutants, and dissolved oxygen (Boano et al., 2014; Grant, Gomez-Velez, and Ghisalberti 2018; Roche et al., 2018). Turbulent flow over permeable walls has been studied using both experiments (Blois et al., 2012; Kim et al., 2018, 2019, 2020; Manes et al., 2009; Manes et al., 2011a; Manes et al., 2011b; Pokrajac and Manes 2009; Roche et al., 2018; Suga et al., 2010; Suga et al., 2017) and numerical simulations (Breugem and Boersma 2005; Breugem et al., 2006; Rosti et al., 2015; Sinha et al., 2017). In these studies, the effects of wall permeability on the structure and dynamics of turbulence across the permeable interface, as well as the link between turbulence inside and outside the wall, have been quantified. Four important modifications have been highlighted compared to flows over impermeable walls with similar interfacial topography: 1) an earlier transition to turbulence (Suga et al., 2010), 2) increased bulk flow resistance (Manes et al. 2009), 3) increased Reynolds shear stress (RSS) contributions from sweep events in the immediate vicinity of the permeable wall (Suga et al., 2011), and 4) enhanced turbulence due to bed permeability (Breugem et al. 2006). While these studies provide a wealth of new understanding concerning the physics of turbulent flows overlying permeable walls, they have focused on a static wall geometry rather than a dynamic wall interface, where the geometry can be altered by processes such as microorganism colonization over a range of timescales. For example, the total biomass, and hence porosity, of the interface may change with the seasons, or

at much smaller scales as individual biofilm streamers move in response to turbulence and that can lead to short-lived fluctuations in the interface porosity.

In almost all aquatic environments, as a result of attachment and colonization of bacteria on solid surfaces, microbial biomass exists in the form of biofilms consisting of a collection of different microscopic organisms living in a self-secreted polymeric matrix (Battin et al., 2007), and that can have profound effects on the flow dynamics. The presence of biofilms can alter flow structure in a number of ways, such as reduced bed porosity due to the presence of biomass in the pores and throats of the pore spaces. Previous studies have shown decreased velocity fluctuations and Reynolds shear stresses with reduced bed porosity (Breugem et al., 2006; Rosti et al., 2015). In addition, the biofilm can modify the geometry of the porous matrix, which is particularly important at the interface between the subsurface and free-flow where changes in surface roughness can affect the flow structure. The combined effects from these factors result in a modified flow structure for flow over biofilm-covered permeable beds.

Biofilm growth may also stabilize sediments and alter the mechanism of sediment entrainment, as well as influencing the generation of bedforms (Frostick and McCave 1979; Lichtman et al. 2018; Malarkey et al. 2015; Parsons et al. 2016; Sutherland, Amos, and Grant 1998; Widdows et al. 2000). Vignaga et al. (2013) showed that bio-stabilized sediment (i.e. biofilm-bound sediment) acts more like a stretched membrane than a collection of loose particles. In gravel-bed rivers, biofilm growth can affect the hydrodynamics of flow and hyporheic exchange by modifying the geometry of the bed interface and the connectivity of subsurface pore spaces. This can, in turn, affect the concentration of oxygen, organic carbon, and other electron acceptors, as well as the biogeochemical reactions occurring inside the bed (Battin et al. 2003; Boano et al. 2014; Dzubakova et al. 2018). However, a limited number of studies have addressed quantitatively the effects of biofilm on flow characteristics, particularly for flow over permeable surfaces. Graba et al. (2010) quantified biomass dynamics during growth and subsequent detachment stages of epilithic biofilms on impermeable rough beds with 20-mm-high hemispherical artificial cobbles in a turbulent flow. They reported a modest decrease in bed shear stress and a decrease in the equivalent sand grain roughness due to smoothing of bottom roughness as a result of biofilm growth. In a follow-up study, Graba et al. (2013) investigated the effect of flow rate and wall shear stress on biomass dynamics and the algal composition of biofilm during growth and detachment stages. They observed a similar trend in wall shear stress with biofilm growth and also reported a direct relationship between biofilm attachment strength and shear stress during biofilm growth. Walker et al. (2013) studied the modification of a turbulent boundary layer developing over a biofilm-covered smooth impermeable surface, such as would relate to the drag on a ship hull. They reported increased skin friction due to biofilm growth on smooth walls. Moreover, a notable finding from their study was that the effective equivalent sand grain roughness of biofilms was greater than their physical roughness, owing to their compliant structure and resulting motion under turbulent flow conditions. In another group of experimental studies, the effect of the presence and growth of biofilm on transport phenomena over and inside porous media has been investigated, showing increased dispersion, longer retention times, and non-Fickian transport with biofilm growth in gravel bed streams (Aubeneau et al., 2016), in packed sphere porous medium (Carrel et al., 2018), and in an open flume with impermeable bed (Roche et al., 2017).

Thus, while biofilms are ubiquitous in aquatic environments, including engineering processing systems and certain natural streams bounded by permeable beds (alluvial rivers), their effect on flow is poorly understood, particularly in the case of flow over permeable walls. This lack of direct measurements represents a knowledge gap that limits our ability to develop reliable predictive models of flow within natural systems such as gravel bed rivers, which are highly permeable and an ideal environment favoring biofilm growth. Specifically, we aim to investigate experimentally the effects induced by the presence of biofilm on flow over idealized permeable beds and explore the differences between freshly grown biofilm and residual biofilm after naturally induced flow-driven partial biofilm detachment. Particle image velocimetry (PIV) is used to quantify the characteristics of turbulent flow over permeable beds with and without biofilms, with the latter serving as a baseline for comparison.

2 Experimental Apparatus

2.1 Flow Facility

A special flow facility was designed and built to accommodate the use of permeable beds with different geometries. The flow facility was a recirculating closed water channel with rectangular $5 \times 8\text{-cm}^2$ cross-section (Figure 1A and B), and consisted of four main components: 1) flow conditioner, 2) boundary-layer development section, 3) test section, and 4) flow diffuser. In order to reduce the turbulence intensity of the incoming flow, the flow conditioner was equipped with a perforated plastic sheet, 3 mesh screens, and a two-dimensional contraction section with inlet to outlet height ratio of 8:1. The boundary-layer development section was 1 m in length followed by a 0.50-m-long test section equipped with glass windows on the two side walls as well as the top wall for optical access. Flow rate was controlled by setting the pump frequency, f , using a variable frequency drive, and discharge was measured using a SeaMetrics EX810P insertion electromagnetic flow meter.

The permeable bed consisted of a regular array of acrylic rods spanning the width of the channel covering both the boundary layer development section and the test section (sections (2) and (3) in Figure 1A). The acrylic rods were secured to two machined perforated acrylic plates with holes for the rods (similar to a pegboard). The bed consisted of four 0.30-m-long individual permeable modules complemented by two 0.15-m-long sections at the two ends of the channel to accommodate the transitions; the first at the inlet (after the contraction) and the second before the diffuser (outlet). The design of these perforated plates allowed the rods to be mounted in two different arrangements and thus obtain two different porosities, 35% and 45%. As shown in Figure 1, the higher porosity was achieved using 6.3 mm (0.25 in) acrylic rods mounted in a square array, while the lower porosity was achieved by adding 3.2 mm (0.125 in) acrylic rods to the center of each square cell, thus reducing the porosity by ~10%. The value for the lower porosity was primarily determined based on cost and construction constraints, yet its porosity was inspired by typical values found in gravel-bed rivers. In all experiments, the porosity of only the last 0.30-m-long permeable bed module, where measurements were made, was varied. This module was located 1.05-m from the channel inlet (Figure 1B). The bed porosity upstream of this measurement module was the same (45%) in all experiments. The reason and implications for this design are further explained in §2.2 and §5.

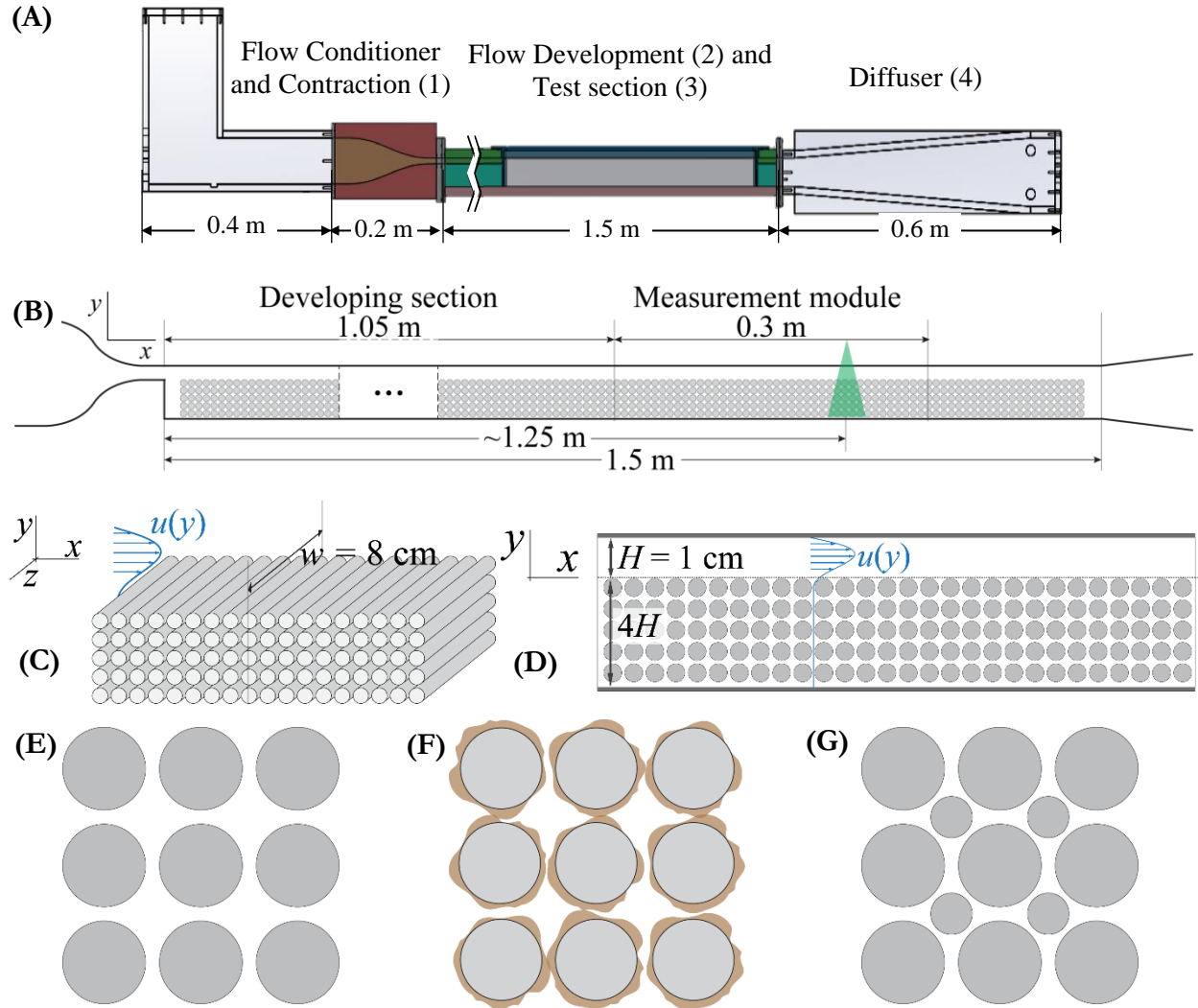


Figure 1. (A) Side view of the water channel consisting of four main components: 1) 0.2-m-long flow conditioner; 2) 1-m-long boundary-layer development section; 3) 0.5-m-long test section optically accessible on three sides through glass windows; and 4) 0.6-m-long flow diffuser. (B) Schematic of channel instrumented with the permeable bed, indicating the location of the PIV measurements at 0.2-m from the beginning of the measurement module. (C) Configuration of the idealized 2D permeable bed placed in the Flow Development and the Test section of the flow facility (Sections 2 and 3 in panel A); (D) Flow domain height including the bed and the free flow portion ($y = 0$ at the top of the cylinders), (E) 45% porosity (Baseline). (F) Schematic representation of biofilm covered bed, and (G) 35% porosity. The diameters of the large and small cylinders were 6.3 mm and 3.2 mm, respectively.

2.1 Biofilm Growth Reactor

2.1.1 Biofilm Reactor

Biofilm was grown on only one of the 0.30-m-long permeable bed modules, hereafter referred to as the measurement module. A dedicated recirculating reactor was designed and built to grow biofilm on the measurement module of the permeable bed under controlled conditions. After completion of biofilm growth, the measurement module was transferred to the water channel and placed in the test section for flow experiments. The decision to develop biofilm *outside* the water channel in a standalone biofilm reactor was made for two practical reasons: 1) to enable

use of the facility while one measurement module was being processed in the reactor; and 2) to avoid both undesired biofilm growth on the channel's glass walls (to preserve optical clarity) and undesired accumulation in portions of the channel with limited access for cleaning. In this regard, biofilm growth on the top wall in the boundary layer development section could have introduced unpredictable effects on the flow characteristics in the channel. Therefore, a transition (see §5) in bed porosity existed at the beginning of the measurement module that resulted in developing flow over the biofilm bed module.

2.1.2 Biofilm Development Protocol

Figure 2A shows schematically the configuration of the reactor. A multi-cassette Cole Parmer MasterFlex L/S peristaltic pump (P1) was used to deliver the electron donor and growth medium at fixed equal flow rates of 4 ml/min. A 250-g/m³ aqueous solution of potassium acetate (KCH₃COO) was used as the electron donor and tap water was used as the growth medium due to its high mineral concentration. A Cole Parmer gear pump (P2) was used for recirculation of the fluids at 40× the combined influent and effluent flow rate (~320 ml/min) to establish fully mixed conditions in the reactor. The resulting average streamwise flow velocity in the reactor, based on the volumetric flow rate and cross-sectional area, was ~4 mm/s. A third cassette on the peristaltic pump was used to extract the effluent from the aeration bottle and maintain a constant fluid level therein. An aeration stone inside the aeration bottle was connected to a low-pressure air supply line to provide oxygen to the reactor. In this manner, the dissolved oxygen levels were maintained close to saturation by compensating for oxygen consumption by biofilm activity.

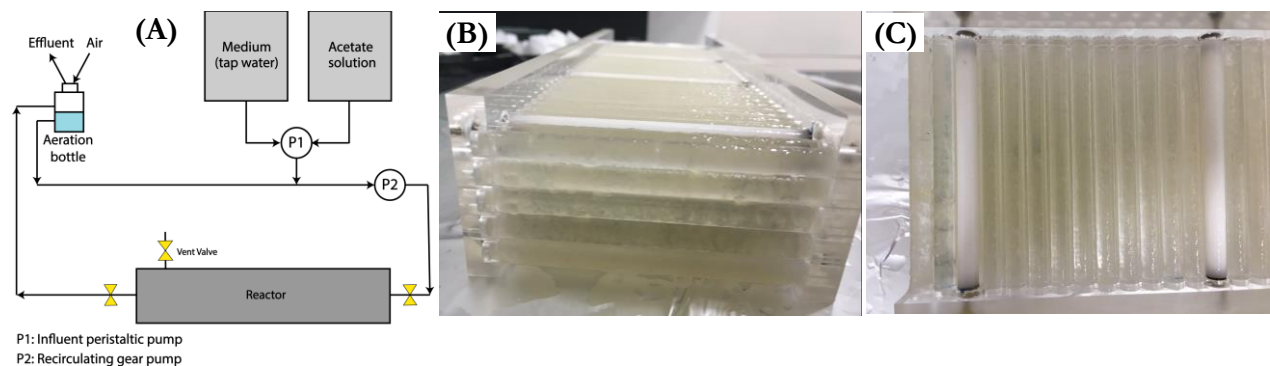


Figure 2. (A) Flow diagram for the recirculating biofilm reactor. (B, C) Biofilm bed section removed from the reactor before being transferred to the flow facility. A multi-cassette Cole Parmer MasterFlex L/S peristaltic pump (P1) was used to deliver the electron donor and growth medium solutions. A Cole Parmer gear pump (P2) was used for recirculation of the fluids to establish fully-mixed conditions in the reactor.

The reactor, with the measurement module of the permeable bed placed inside, was inoculated with activated sludge from a local wastewater treatment plant. Biofilm was allowed to grow on the cylinders for 14 days. During this time period, the biofilm was exposed to room light for approximately 6–10 hours each day. Based on the inoculum and growth conditions, the dominant members in this biofilm were heterotrophic and nitrifying bacteria whose growth is relatively insensitive to light conditions. The reactor was maintained at a room temperature of 20–22°C. After the 14-day growth period, the biofilm-covered measurement module was removed from the reactor and its sidewalls above the top layer of the cylinders were cleaned carefully without disturbing the biofilm to ensure unhindered optical access. This module was then transferred to

the flow facility for flow experiments. Figure 2B and C show the biofilm-covered bed before being placed in the water channel. As already mentioned, since biofilm growth was limited to the reactor-processed portion of the bed section (measurement module), a transition in bed porosity and roughness geometry existed at the ends of this section. The effect of this transition on flow development is discussed in §5.

2.2 PIV Setup

A dual-head, pulsed, Evergreen Nd:YAG laser with maximum energy of 200 mJ/pulse was used to form a ~1-mm-thick laser sheet to illuminate the tracer particles in the streamwise–wall-normal (x – y) plane at the section centerline. The longitudinal position of the light sheet was 1.25 m downstream of the channel inlet and approximately 0.20 m from the beginning of the measurement module (Figure 1B). A 16-bit, Andor Neo sCMOS camera with 5.5-megapixel (2560×2160 -pixel array) sensor and a pixel size of $6.5 \mu\text{m}$ was used to capture image pairs at a rate of 10 Hz. The camera was coupled with a Navitar long-distance microscope with numerical aperture (NA) of ~0.012, consisting of a $0.25\times$ objective, a $2\times$ adapter, and a zoom lens set at $\sim 2\times$ resulting in a magnification of $\sim 1.1\times$ translating to $\sim 7 \mu\text{m}/\text{pixel}$, and a resolution of $\sim 40 \mu\text{m}$ at 550 nm wavelength. The field of view of the imaging setup was $\sim 18 \times 14 \text{ mm}^2$. The FOV covered up to $\sim 7 \text{ mm}$ above the cylinder tops, in order to avoid error from optical aberrations observed near the top of the FOV. Fluorescent particles ~ 10 – $15 \mu\text{m}$ in diameter were introduced into the flow as tracers and their fluoresced light was recorded through a long-pass 550 nm filter. Raw PIV images were processed with LaVision DaVis 8.2 software using a sequential cross-correlation algorithm with a final interrogation window size of 64^2 pixels with 50% overlap, resulting in a vector field resolution of $\sim 0.44 \text{ mm}$ and a vector grid spacing of $\sim 0.22 \text{ mm}$ ($0.035d$).

2.3 Experiments

Five sets of experiments were conducted – two without biofilm (*nBF*) and three with biofilm-covered bed sections (*BF*). The flow over the bed with 45% porosity throughout the channel without biofilm (*nBF*-45%) had no geometrical transition and was used as a baseline reference case for comparison. The other dataset without biofilm was *nBF*-45-35% where the bed porosity was 45% in the developing section transitioned to a 0.30-m-long measurement module with 35% porosity (Figure 1B). Lastly, the *BF* datasets correspond to experiments on different batches of biofilm developed independently at different times on the 45%-porosity measurement module. As such, the 45% bed porosity in the channel in all flow experiments transitioned to the 0.30-m-long biofilm-covered measurement module, whose porosity was assumed smaller than 45% due to presence of biomass. The location of all PIV measurements was 0.20 m downstream from the beginning of the measurement module. Details of the experimental beds are presented in Table 1.

Table 1. Dataset Summary

Dataset	Biofilm	Description
<i>nBF</i> -45% (reference)	No	45% bed porosity in the boundary-layer development and measurement module.
<i>nBF</i> -45-35%	No	45% bed porosity in the boundary-layer development section, and 35% porosity in the measurement module.
<i>BF1</i>	Yes	45% bed porosity in clean conditions (before biofilm growth; the
<i>BF2</i>	Yes	<i>actual</i> porosity in the biofilm section is likely lower due to presence

BF3

Yes

of biofilm). These correspond to three different batches of biofilm developed independently at different times in the same reactor.

Temporal decomposition of the velocity field, $\mathbf{u}(x,y,t) = (u(x,y,t), v(x,y,t))$, was performed as $u = \bar{u} + u'$, where the overbar denotes time-averaged (Reynolds-averaged or mean) values and the prime denotes the deviation from the time-averaged value. Line averaging in the streamwise direction (x -direction) at any vertical position y , was performed according to the definition given by Nikora et al. (2001). For example, for mean streamwise velocity, \bar{u} :

$$\langle \bar{u} \rangle(y) = \left(\int_{A_f} \bar{u}(x', y) dx' \right) / A_f \quad (1)$$

where A_f is the area occupied by fluid at any vertical position, y , and is determined based on the number of vectors at each y location. In addition, the spatial deviation was calculated as the difference between the time-averaged and double-averaged quantities, $\tilde{u} = \bar{u} - \langle \bar{u} \rangle$.

Figure 3 shows a representative time-averaged velocity field, with streamwise velocity \bar{u} contours and streamlines (Figure 3A), in addition to the corresponding double-averaged velocity profile, $\langle \bar{u} \rangle(y)$, (Figure 3B). Due to flow detachment, a recirculation region exists between the cylinders that results in negative streamwise velocities with a velocity magnitude of $\sim 0.1 U_{max}$. Similar to observations by Breugem et al., (2006), the line-averaged velocity profile, $\langle \bar{u} \rangle$, exhibits an inflection point just below the interface, denoted as y_{inflec} . The PIV uncertainty in particle displacement calculated from the images is 5% of the particle image diameter, or ~ 0.1 pixels ($\sim 1.4 \times 10^{-3}$ mm in the measurement plane). For the different laser pulse time delays used herein, this equates to a velocity uncertainty of $\sim 0.4\%$ of U_{max} in each case.

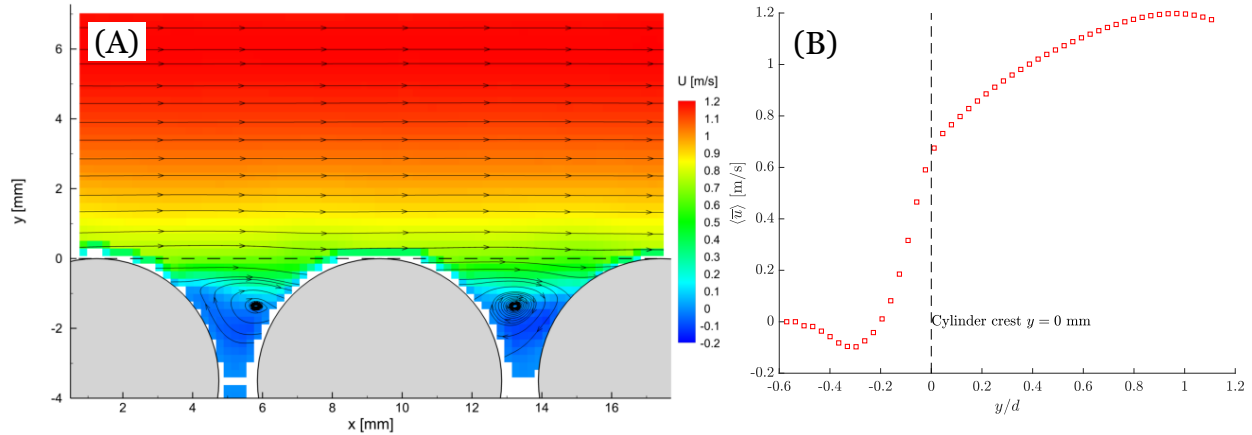


Figure 3. (A) Time-averaged streamwise velocity, \bar{u} , (B) double-averaged velocity profile at $Re \approx 7000$. Dashed line indicates the top of the cylinders at $y = 0$ mm, and $d = 6.3$ mm is the cylinder diameter.

The total shear stress, τ , is calculated as the sum of viscous, Reynolds, and dispersive (form-induced) shear stresses:

$$\tau = \mu \frac{d\langle \bar{u} \rangle}{dy} - \rho \langle \bar{u}'v' \rangle - \rho \langle \tilde{u}\tilde{v} \rangle. \quad (2)$$

Figure 4 presents the total shear stress as well as the individual terms in Eq. (2), normalized with wall shear stress τ_w^p . The shear stress does not include the drag term below the cylinder crest ($y/d < 0$). The shear stress at the permeable wall, τ_w^p , was calculated by extrapolating the linear

segment of the total shear stress profile (Eq. (2) with density, $\rho = 997.5 \text{ kg/m}^3$ and viscosity, $\mu = 0.9321 \times 10^{-3} \text{ Pa.s}$) near the channel centerline to the crest location ($y = 0$).

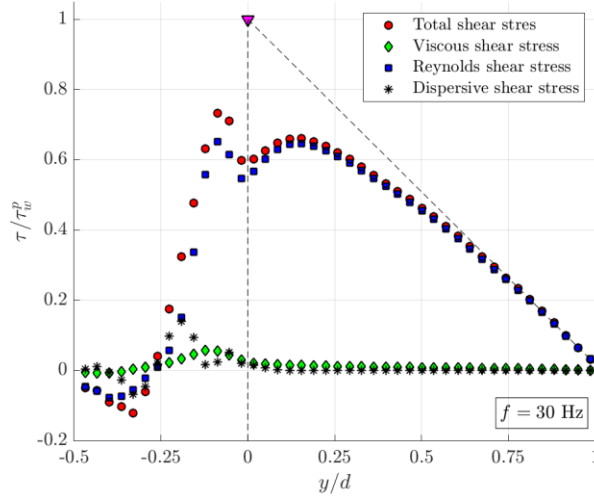


Figure 4. Example of contributions of individual terms to total shear stress and extrapolation for estimation of wall shear stress.

Table 2 presents details of the experimental conditions for different runs and datasets. Discharge, Q , was directly measured by the flowmeter, while U_{max} and y_{max} were obtained from the double-averaged velocity profiles. The bulk Reynolds number, Re , for this flow configuration is defined as:

$$Re = \frac{U_b H}{\nu}, \quad (3)$$

where H is the channel height (0.01 m for all cases), $\nu = 0.934 \times 10^{-3} \text{ m}^2/\text{s}$ is the kinematic viscosity of water, and U_b is the bulk velocity calculated as the average velocity for $0 \leq y \leq H$, as defined by Breugem et al. (2006). Since the velocity field is resolved up to $y \approx 7 \text{ mm}$, a fourth-order polynomial curve fit was used to approximate the velocity profile up to the top wall ($y = 10 \text{ mm}$) for calculation of U_b . The friction velocity (u_τ^p) and friction Reynolds number (Re_τ^p) are defined as:

$$u_\tau^p = \sqrt{\tau_w^p / \rho}, \quad (4)$$

$$Re_\tau^p = \frac{u_\tau^p H}{\nu}. \quad (5)$$

The permeability Reynolds number (Re_K) was calculated as,

$$Re_K = \frac{u_\tau^p \sqrt{K}}{\nu} \quad (6)$$

where K is the bed permeability, which is estimated from the Kozeny–Carman equation for cylinders in cross-flow (Nakayama et al., 2007) as,

$$K = \frac{\phi^3 d_h^2}{144(1 - \phi)^2} \quad (7)$$

where ϕ is porosity and d_h is the pore hydraulic diameter. This calculation yields a permeability of 0.087 mm^2 and 0.051 mm^2 for the beds with 45% and 35% porosity, respectively. As a first

approximation for the bed with biofilm, we used the same permeability value as the low-porosity bed.

For sufficiently high Reynolds number, a logarithmic layer is expected in the boundary layer above the permeable bed. A common parametrization of the log law is

$$\langle \bar{u} \rangle^+ = \frac{1}{\kappa} \ln \left(\frac{y^+ + y_0^+}{k_s^+} \right), \quad (8)$$

where $\langle \bar{u} \rangle^+ = \langle \bar{u} \rangle / u_\tau^p$, κ is the equivalent von Kármán constant (Breugem et al. 2006; Fang et al. 2018), y^+ is the vertical distance above the cylinder crest, y_0^+ is the zero-displacement height, and k_s^+ is the equivalent roughness height, all normalized with viscous length scale $y^* = \nu / u_\tau^p$.

In experiments with biofilm, the pump frequency, f , and thus channel flow rate, Q , were increased in steps, and data were recorded for $f = 4.5$ Hz and 8 Hz ($Q \approx 0.18$ and 0.28 L/s), before reaching the target of 16 Hz and 30 Hz ($Q \approx 0.54$ and 0.95 L/s). After recording data for the highest flow rate, the pump frequency was reduced, and data was recorded sequentially at $f = 8$ Hz and 4.5 Hz ($Q \approx 2.8$ L/s and $Q \approx 0.18$ L/s) (with the exception of the *BF3* dataset). Figure 5 illustrates the flow rate ramping stages schematically. The number of image pairs for each flow setting and the corresponding number of flow-through times is given in Table 3. The flow-through time was calculated as the ratio of the streamwise length (18 mm) of the field of view to the bulk velocity (U_b). After each stage, there was at least a 2-minute wait time before recording images. The flow characteristics during ramp up and ramp-down in flow discharge, referred to as *before detachment* (BD) and *after detachment* (AD), respectively, are compared later to illustrate the effect of biofilm detachment on flow behavior.

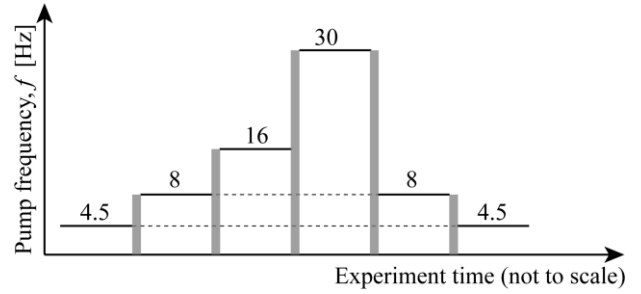


Figure 5. Schematic of flow rate ramping stages in the flow facility. The shaded regions represent wait time before recording images.

2.4 Flow Characteristics and Variability due to Biofilm Presence

Despite maintaining very similar experimental conditions in the three flow experiments conducted in the presence of biofilm, due to unavoidable differences in biofilm growth, the flow was inherently subject to some degree of variability. Under these conditions, data repeatability was difficult to achieve. As such, the first step in the present analysis was to characterize statistically the boundary layer by computing the ensemble-averaged profiles and quantifying the variability between the three different sets of experiments. The results presented from biofilm experiments, unless noted otherwise, are the average of the three separate experimental datasets: *BF1*, *BF2* and *BF3* in Table 2, and the error bars for flow over the biofilm beds represent the range of measurements.

Table 2. Experimental conditions: f is pump frequency, Q is volumetric flow rate, U_b is bulk velocity, U_{max} is maximum streamwise velocity, y_{max} is the coordinate where U_{max} occurs, u_τ^p is the friction velocity at the permeable wall (Eq. 4), Re is the bulk Reynolds number (Eq. 2), and Re_τ^p is the friction Reynolds number at the permeable wall (Eq. 5), and Re_K is the permeability Reynolds number (Eq. 6). k_s^+ , y_0^+ and κ are the equivalent roughness height and zero displacement height (normalized with viscous wall units y^*) and von Kármán constant, respectively, from a logarithmic fit to the velocity profile (Eq. 8). BD and AD indicate “before detachment” and “after detachment” respectively.

Dataset	f [Hz]	Q [L/s]	U_b [m/s]	U_{max} [m/s]	y_{max} [mm]	$u_\tau^p \times 10^{-3}$ [m/s]	Re	Re_τ^p	Re_K	k_s^+	y_0^+	κ
nBF-45%	4.5	0.173	0.150	0.186	5.3	14.1	1609	150	4.4	0.4	4.5	0.40
	8	0.293	0.259	0.315	5.9	24.5	2776	262	7.7	2.9	28.3	0.31
	16	0.534	0.504	0.615	6.2	46.7	5396	500	14.8	13.4	81.0	0.25
	30	0.971	0.979	1.198	6.2	82.1	10481	879	25.9	23.7	140.6	0.22
nBF-45-35%	4.5	0.177	0.151	0.191	5.2	14.3	1612	153	3.5	0.9	13.2	0.33
	8	0.293	0.267	0.322	5.6	23.2	2860	249	5.6	3.2	33.8	0.28
	16	0.536	0.516	0.639	6.0	46.6	5526	499	11.3	13.1	88.8	0.24
	30	0.953	0.976	1.217	6.0	89.3	10440	956	21.6	35.9	179.7	0.22
BF1	BD 4.5	0.177	0.168	0.213	5.9	20.1	1797	215	4.9	5.5	28.0	0.31
	BD 8	0.284	0.298	0.379	6.6	35.2	3186	377	8.5	14.0	52.7	0.28
	16	0.543	0.585	0.757	6.8	69.1	6260	739	16.7	60.9	152.3	0.21
	30	0.953	1.111	1.403	6.6	106.2	11886	1137	25.7	50.4	172.8	0.21
	AD 8	0.291	0.299	0.368	6.3	29.3	3195	314	7.1	4.1	30.7	0.31
	AD 4.5	0.173	0.167	0.209	5.7	15.9	1789	170	3.8	0.4	3.4	0.41
BF2	BD 4.5	0.178	0.162	0.205	5.6	17.7	1730	189	4.3	4.3	29.9	0.29
	BD 8	0.281	0.283	0.355	6.0	32.0	3030	343	7.7	13.6	68.6	0.26
	16	0.536	0.563	0.701	6.3	58.7	6030	629	14.2	39.6	165	0.21
	30	0.953	1.029	1.296	6.3	102	11020	1093	24.6	44.4	208	0.23
	AD 8	0.287	0.280	0.344	5.8	26.2	3000	281	6.3	5.9	51.6	0.27
	AD 4.5	0.178	0.158	0.198	5.2	15.3	1690	163	3.7	0.8	14.4	0.36
BF3	16	0.539	0.557	0.685	5.9	51.9	5965	555	12.5	11.0	105.4	0.27
	30	0.946	1.014	1.263	6.1	91.6	10849	981	22.1	34.5	213.8	0.22

Table 3. PIV ensemble size (number of image pairs)

Pump frequency, f [Hz]	Ensemble size	Number of flow- through times
4.5	750	~650
8	1000	~1500
16	3000	~8670
30	4000	~21780

3 Results

The results and analysis presented in the following sections are focused on $f = 4.5$ Hz ($Re = 1700 \pm 100$) and $f = 30$ Hz ($Re = 11150 \pm 700$), selected to illustrate the main trends observed in the data. Similar behavior was observed for the two intermediate flow rates, so these results are not presented for brevity. In order to facilitate comparison, flow and turbulence variables are presented in dimensionless form: streamwise and wall-normal velocity components are normalized with bulk velocity, U_b , and Reynolds and form-induced stresses are normalized with $(u_\tau^p)^2$.

3.1 Biofilm Detachment

3.1.1 Imaging Analysis

The flow experiments in the water channel were conducted at different flow rates where the biofilm was subjected to increased shear stress in several incremental stages (Figure 5). This led to progressive detachment of the biofilm from the solid surfaces. For each flow rate, the extent of biofilm that remained attached to the cylinders was measured using a semi-quantitative image processing method applied to the raw PIV images. At each image pixel, the maximum and minimum pixel intensity within each time series was identified. Next, a map of the difference, or *range*, between these two values at each pixel ($range = max - min$) was generated. The low values in this map correspond to portions of the image where particles cannot be present; i.e. the solid cylinder and biofilm, whereas the high values correspond to regions of the image where tracer particles were present intermittently. The *range* image for the highest pump frequency, $f = 30$ Hz ($Re = 11150 \pm 700$), in each dataset was taken as the reference since after this flow stage nearly all biofilm on the top row of cylinders was detached and its visible biofilm coverage in the top layer was nearly non-existent. The difference calculated with respect to this reference image, and binarized subsequently, depicts the biofilm coverage on the cylinders.

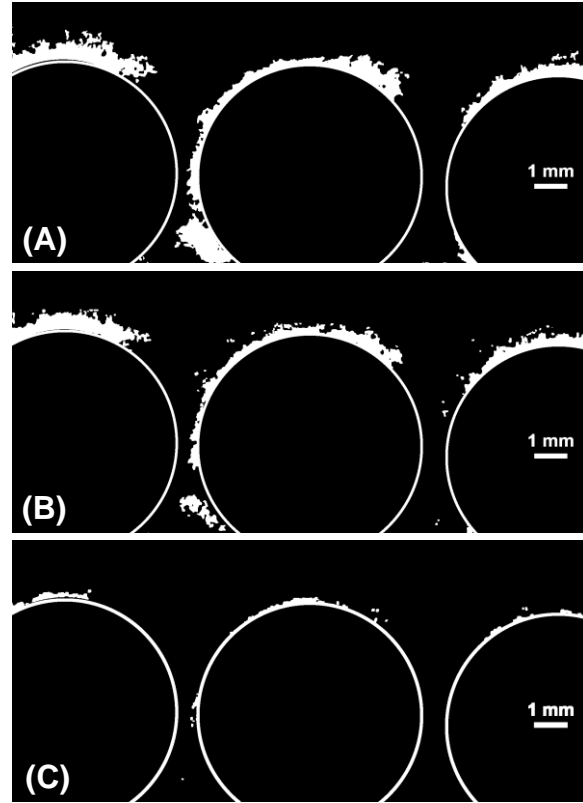


Figure 6. Biofilm coverage at different Re during the ramp-up stage (A) $f = 4.5$ Hz ($Re = 1700 \pm 100$), (B) $f = 8$ Hz ($Re = 3000 \pm 200$), (C) $f = 16$ Hz ($Re = 5800 \pm 400$). The cylinders are outlined in white and a 1-mm scale bar is shown for reference.

Figure 6 shows the biofilm imaged using this method for a representative dataset. At the beginning of the experiment with the lowest flow rate, $f = 4.5$ Hz ($Re = 1700 \pm 100$), the biofilm was in a nearly-pristine condition (Figure 6A), which is consistent with insignificant detachment owing to relatively low wall shear stress. As the flow rate was increased, at $f = 8$ Hz ($Re = 3000 \pm 200$), a modest amount of biofilm detachment was observed (Figure 6B). Finally, at the second highest pump frequency of $f = 16$ Hz ($Re = 5800 \pm 400$), the biofilm coverage was dramatically reduced (Figure 6C). It should be noted that in this way, the biofilm was visualized *indirectly* using the fluorescent particles in raw PIV images. Nevertheless, this method does yield a qualitative picture of the biofilm coverage, since at the end of the experiment biofilm coverage on the top of the cylinders appeared minimal and barely visible to the naked eye. Based on the *range* images, the biofilm thickness on the cylinder crests can be estimated as *c.* 0.5–1 mm, 0.25–0.75 mm, and 0.1–0.25 mm at 4.5 Hz, 8 Hz, and 16 Hz, respectively.

3.1.2 Effect of Biofilm Detachment on Flow Statistics

Results for flow over beds with different biofilm conditions were compared to quantify the effect of biofilm presence and biofilm detachment. Comparisons were made at the pump frequency of

$f = 4.5$ Hz ($Re = 1700 \pm 100$) at the beginning and end of each run, corresponding to ramp-up and ramp-down of flow discharge, respectively (c.f. Figure 5). The lowest pump frequency was selected for this purpose because of the near-pristine condition of the biofilm at the beginning of the experiment, and hence the largest difference in biofilm coverage before and after detachment. Figures 7 and 8 compare double-averaged flow statistics for three cases: no biofilm (nBF-45%), biofilm before detachment (BF-BD), and biofilm after detachment (BF-AD). The biofilm data is the average of two independent runs (BF1 and BF2), and the error bars indicate the data range.

Double-averaged streamwise and wall-normal velocity profiles, normalized with bulk velocity, U_b are presented (Figure 7). The streamwise velocity profile for flow over the beds with and without biofilm at the same flow rate are very similar. One small difference is the slight increase in the maximum streamwise velocity of the free flow (U_{max}/U_b) in the presence of biofilm (Figure 7A). The wall-normal velocity (Figure 7B), showed an upward motion below the cylinder crests for both BD and AD which was not observed for nBF.

The dimensionless streamwise Reynolds normal stress, $\langle \overline{u'u'} \rangle / (u_\tau^p)^2$, at constant pump frequency (Figure 8A) collapsed for $0.5 \lesssim y/d \lesssim 1$. Closer to the bed interface, for $0 \lesssim y/d \lesssim 0.5$, the stress was highest for the bed without biofilm (nBF) and lowest for biofilm before detachment (BF-BD). The maximum stress occurred at $y/d \approx 0$ for all configurations.

The dimensionless wall-normal Reynolds normal stress, $\langle \overline{v'v'} \rangle / (u_\tau^p)^2$, at constant pump frequency (Figure 8B) collapsed for $0.4 \lesssim y/d \lesssim 1$. Close to the bed, for $0 \lesssim y/d \lesssim 0.4$, and similar to the streamwise Reynolds normal stress, the non-biofilm bed had the highest stress, although the differences were very minor. The peak stress for both nBF and BF-AD occurred at $y/d \approx 0.25$, while the peak for BF-BD occurred slightly higher at $y/d \approx 0.3$.

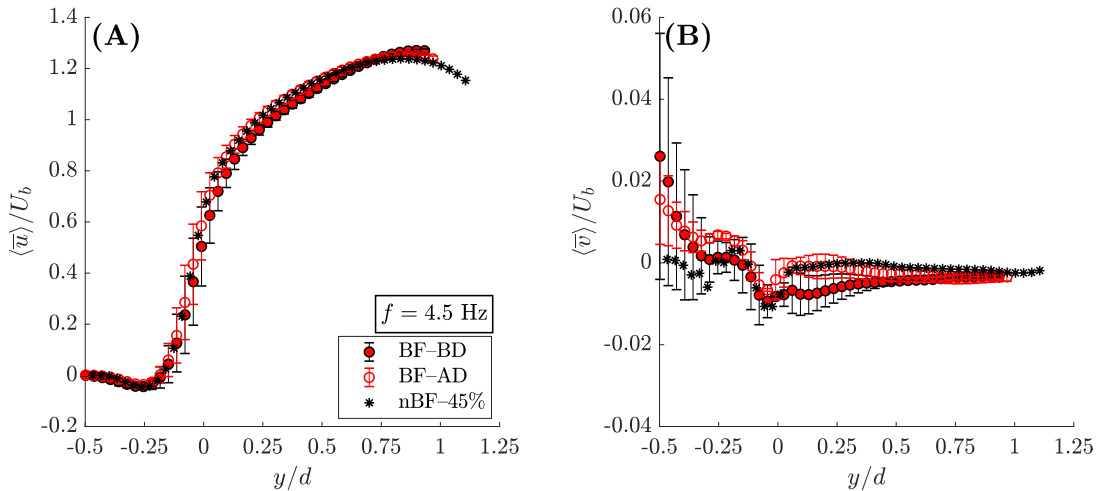


Figure 7. Effect of biofilm detachment on (A) streamwise, and (B) wall-normal velocity for $f = 4.5$ Hz ($Re = 1700 \pm 100$). Biofilm before detachment (BF-BD, filled red circle), and after detachment (BF-AD, open red circle), no biofilm (black asterisk). The error bars indicate the range of data for biofilm datasets. The biofilm data (“BF-BD” and “BF-AD”) are from *BF1* and *BF2* datasets.

Consistent with the other components of Reynolds stress presented herein, the dimensionless Reynolds shear stress, $-\langle \overline{u'v'} \rangle / (u_\tau^p)^2$, was highest for the bed without biofilm in the range

0 $\lesssim y/d \lesssim 0.5$ (Figure 8C). The profiles collapsed for $0.5 \lesssim y/d \lesssim 1$, although within this range, the BF-BD cases had slightly higher values of Reynolds shear stress. The biofilm before and after detachment had highly similar profiles, except in the region $-0.1 \lesssim y/d \lesssim 0.3$ where the normalized RSS after detachment (AD) was higher by approximately 10%. The peak for nBF-45% was at $y/d \approx 0$, whereas the peak for both BF-BD and BF-AD occurred at $y/d \approx 0.18$.

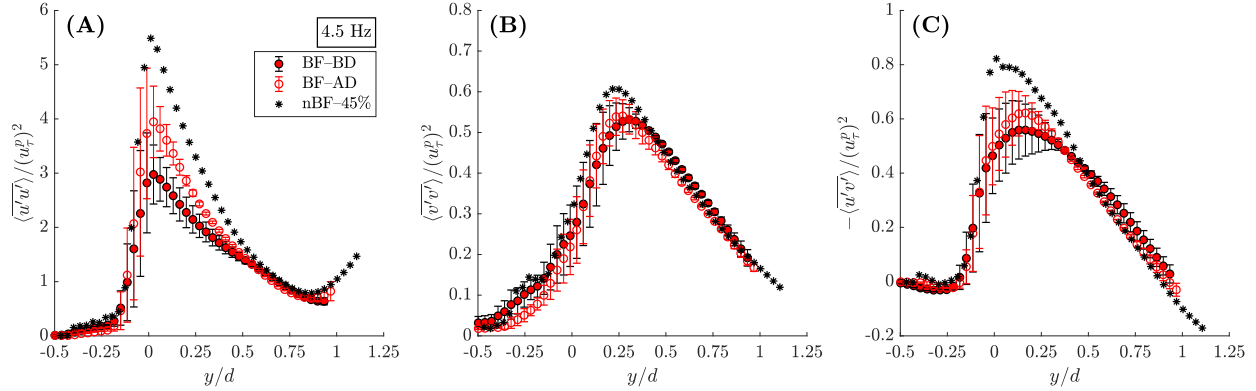


Figure 8. Effect of biofilm presence and subsequent detachment on dimensionless Reynolds stresses. (A) streamwise Reynolds normal stress, (B) wall-normal Reynolds normal stress, and (C) Reynolds shear stress. Biofilm before detachment (BF-BD, filled red circle), biofilm after detachment (BF-AD, open red circle), no biofilm (nBF, black asterisk). The error bars indicate the range of data for biofilm datasets.

3.2 Biofilm and Reduced Bed Porosity

One of the potential effects of biofilm growth in a porous bed is a reduction of porosity likely concomitant with reduction in permeability due to blocking of the pores. As described in the previous section, biofilm detachment occurred due to flow shear during experiments. Since shear stress above the bed is significantly larger than within the bed, detachment is expected to occur mostly in the top layers of the bed, while biomass in the bottom layers of the bed are likely to be less affected. It is reasonable to conjecture that the effects described in §3.1.2 were, at least in part, induced by this reduction in pore space size that was maintained even after the ramp-up phase of the experiment, as qualitatively observed in §3.1.1. In an attempt to replicate the effect of reduced bed porosity associated with biofilm presence, and thus test this hypothesis, flow measurements were performed using a permeable bed section with no biofilm but with a lower porosity. In this manner, the experiments aimed to decouple any changing bed porosity from other effects arising from the presence of biofilms, such as roughness and dynamic geometry. Given that the porosity of the bed with biofilm was not quantified, only *partial* decoupling was possible. It should be noted that, in order to maintain the incoming flow configuration as close to the case of flow with biofilm as possible, the porosity of boundary layer development section of the bed was kept at 45%, and only in the test section was porosity reduced to 35%. This transition (see §5) at the beginning of the measurement module likely affected development of the boundary layer. However, it should be emphasized that the experiments performed herein were not intended to produce universally applicable results, but instead provide valuable direct quantitative comparisons with the baseline case (nBF-45%) in order to assess first-order biofilm effects.

The double-averaged profiles of streamwise and wall-normal velocity for the two non-biofilm datasets (nBF-45% and nBF-45-35%), and the biofilm averaged data are presented in Figure 9.

The streamwise velocity profiles are similar and collapse in the outer layer ($0.5 \lesssim y/d \lesssim 1$) for both biofilm and non-biofilm beds. Variations are evident among the biofilm datasets in the inner layer and slightly below the cylinder crest for $-0.2 \lesssim y/d \lesssim 0.5$.

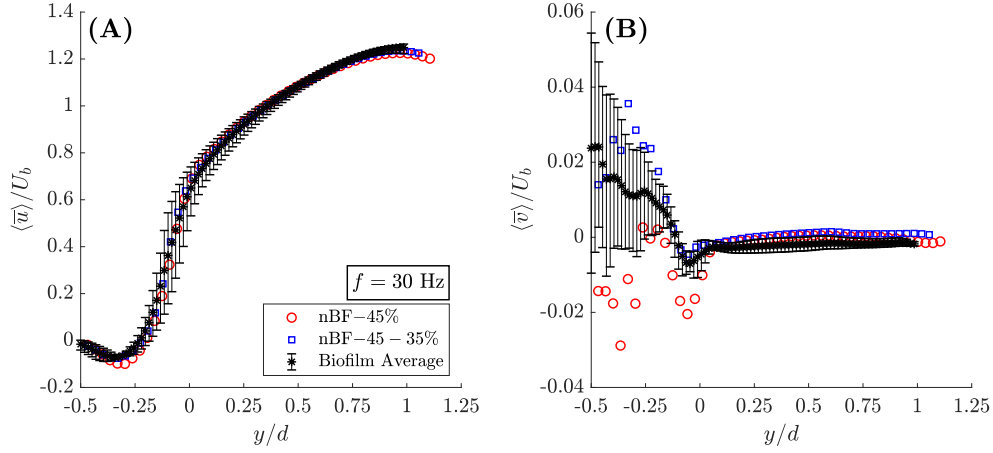


Figure 9. Biofilm effect comparison with reduced bed porosity on streamwise velocity (A), and wall-normal velocity (B) for 30 Hz ($Re = 11150 \pm 700$). No biofilm with 45% bed porosity (red circle), no biofilm with 45% porosity in the flow developing section and 35% in the test section (blue square), biofilm (black asterisk). The error bars indicate the range of data for biofilm datasets.

The wall-normal velocity above the cylinder crest ($y/d > 0$) for all datasets shows a near zero velocity, indicating purely horizontal flow. However, there was an upward velocity below the cylinder-tops ($y/d < 0$) for both the reduced porosity bed (nBF-45-35%) and the biofilm bed. This behavior was also observed before and after-detachment at $f = 4.5$ Hz (Figure 7B).

The log law (Eq. (8)) was fitted to the double-averaged streamwise velocity profiles following the method of Fang et al. (2018) as presented in Figure 10. The fitting parameters for all datasets are provided in Table 2. The results show an increased equivalent wall roughness height k_s^+ and y_0^+ for the biofilm bed compared to the two non-biofilm cases.

Figure 11 presents the double-averaged dimensionless Reynolds stresses for the two datasets without biofilm (nBF-45% and nBF-45-35%), along with the biofilm average. A common feature of the profiles presented herein is that at fixed pump frequency individual Reynolds stress components (streamwise, wall-normal, and shear) normalized with $(u_\tau^p)^2$ collapse for all bed configurations in the outer layer $0.25 - 0.4 \lesssim y/d \lesssim 1$. Near the permeable bed

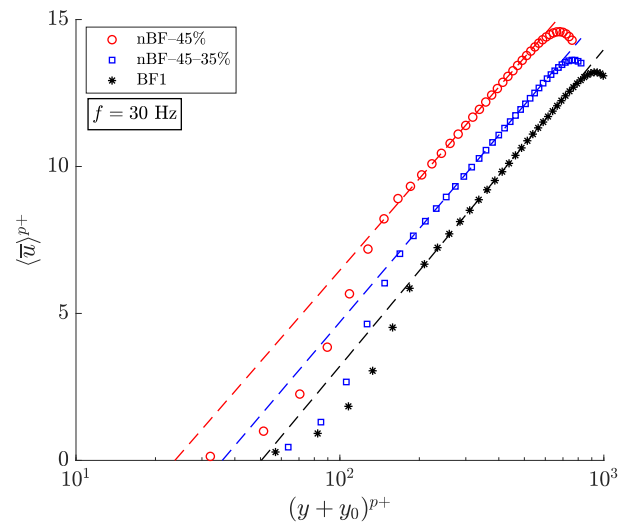


Figure 10. Logarithmic fit to the double-averaged streamwise velocity profiles for 30 Hz pump frequency ($Re = 11150 \pm 700$). Red: $k_s^+ = 23.7$ for $y^+ \in [83 \ 350]$, Blue: $k_s^+ = 35.9$ for $y^+ \in [52 \ 388]$, Black: $k_s^+ = 50.4$ for $y^+ \in [112 \ 492]$. Refer to Table 1 for detailed dataset information.

($0 \lesssim y/d \lesssim 0.25$) the reference non-biofilm case (nBF-45%) has the highest stress. Moreover, the non-biofilm reduced porosity bed (nBF-45-35%) and the biofilm average show quite similar profiles at nearly all y positions.

The dimensionless streamwise Reynolds normal stress, $\langle \overline{u'u'} \rangle / (u_\tau^p)^2$, collapsed for $0.25 \lesssim y/d \lesssim 1$ for the three bed configurations (Figure 11A). In addition, the maximum streamwise Reynolds normal stress occurred slightly below the crest at $y/d \approx -0.1$ for all flow configurations. However, while the reference non-biofilm bed (nBF-45%) reflects a prominent peak, the reduced porosity non-biofilm bed (nBF-45-35%) and the biofilm bed (BF) had nearly flat and highly similar profiles within the region $-0.1 \lesssim y/d \lesssim 0.25$. Within this range, the nBF-45% bed had the highest magnitude of $\langle \overline{u'u'} \rangle / (u_\tau^p)^2$.

The dimensionless wall-normal Reynolds normal stress, $\langle \overline{v'v'} \rangle / (u_\tau^p)^2$, for the three bed configurations collapsed for $y/d \gtrsim 0.4$ (Figure 11B). For $-0.5 \lesssim y/d \lesssim 0.3$, the reference non-biofilm bed (nBF-45%) had the highest stress values. In addition, nBF-45% had a maximum below the cylinder crests at $y/d \approx -0.1$, while BF and nBF-45-35% attained their maximum above the bed at $y/d \approx 0.2$. The non-biofilm reduced porosity bed (nBF-45-35%) and the biofilm average had nearly identical profiles for all y positions.

The dimensionless Reynolds shear stress profiles, $-\langle \overline{u'v'} \rangle / (u_\tau^p)^2$, demonstrate a trend similar to the other Reynolds stress components, where the profiles collapsed for $y/d \gtrsim 0.4$ (Figure 11C). For

$-0.2 \lesssim y/d \lesssim 0.4$, nBF-45% had the highest stress compared to the two other datasets. Moreover, while the reduced porosity non-biofilm bed (nBF-45-35%) and the biofilm bed had relatively flat profiles for $-0.1 \lesssim y/d \lesssim 0.25$ and a maximum near $y/d \approx 0.2$, the reference non-biofilm bed (nBF-45%) had a prominent peak at $y/d \approx -0.1$.

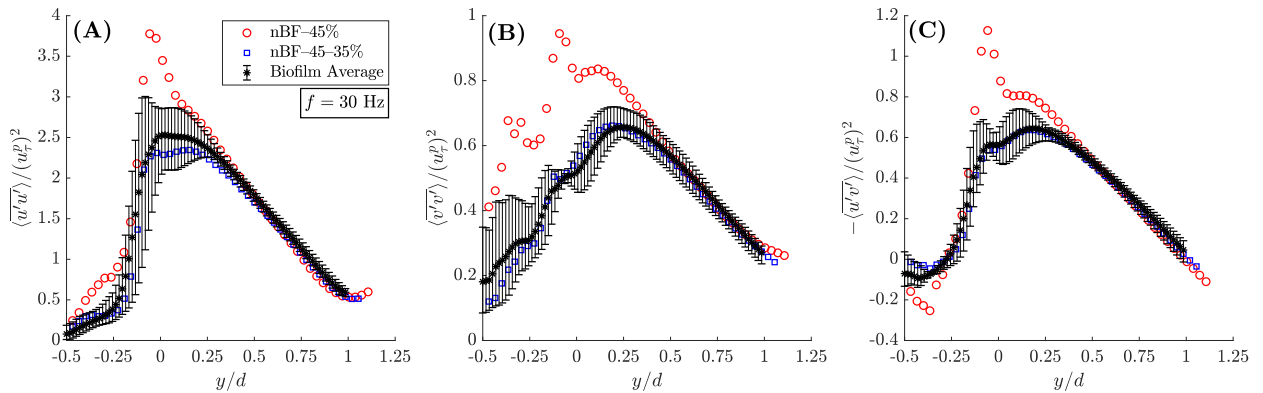


Figure 11. Biofilm effect comparison with reduced bed porosity for $f = 30$ Hz ($Re = 11150 \pm 700$). (A) streamwise Reynolds normal stress, (B) wall-normal Reynolds normal stress, and (C) Reynolds shear stress. No biofilm with 45% bed porosity (red circle), no biofilm with 45% porosity in the flow developing section and 35% in the test section (blue square), biofilm (black asterisk). The error bars indicate the range of data for biofilm datasets.

The form-induced (dispersive) stresses are presented in Figure 12. In all cases, the form-induced stresses are very small directly above the cylinder crests ($0 \lesssim y/d \lesssim 0.25$) and practically zero for $y/d \gtrsim 0.25$. Comparing Figures 11 and 12 reveals that above the cylinder crests, the form-induced stresses are negligible compared to the Reynolds stresses. However, below the crests (–

0.5 $\lesssim y/d \lesssim 0$) the form-induced stresses are comparable to the Reynolds stresses in their magnitude and cannot be neglected.

The streamwise, form-induced, normal stresses attain their peak at $y/d \approx -0.12$, with a magnitude comparable to that of the corresponding local Reynolds stress (Figure 12A). The wall-normal, form-induced, normal stresses attain their maximum at $y/d \approx -0.3$, where the peak value is even greater than the corresponding local Reynolds stress (Figure 12B). Lastly, the form-induced shear stress showed a behavior and range similar to the Reynolds shear stress within the region $-0.5 \lesssim y/d \lesssim 0$ range (Figure 12C). For all components of the form-induced stress, the biofilm datasets demonstrate a broad range of variation that was not observed in the Reynolds stresses.

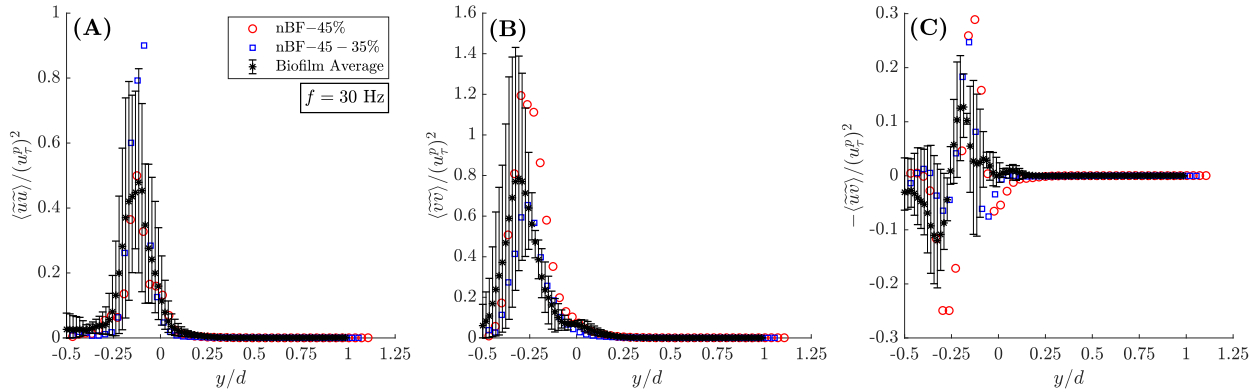


Figure 12. Biofilm effect comparison with reduced bed porosity for $f = 30 \text{ Hz}$ ($Re = 11150 \pm 700$). (A) streamwise form-induced normal stress, (B) wall-normal form-induced normal stress, and (C) form-induced shear stress. No biofilm with 45% bed porosity (red circle), no biofilm with 45% porosity in the flow developing section and 35% in the test section (blue square), biofilm (black asterisk). The error bars indicate the range of data for biofilm datasets. ($Re = 11150 \pm 700$),

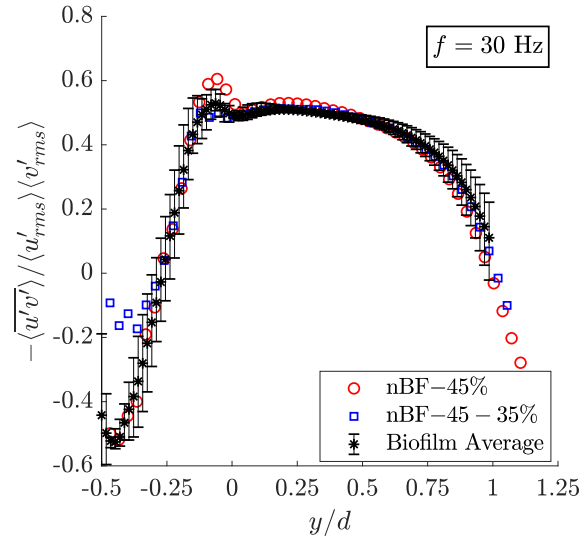


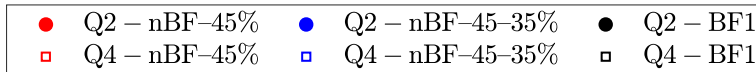
Figure 13. Biofilm effect comparison with reduced bed porosity on correlation coefficient of velocity fluctuations for $f = 30 \text{ Hz}$ ($Re = 11150 \pm 700$). No biofilm with 45% bed porosity (red circle), no biofilm with 45% porosity in

The correlation coefficient $(-\overline{u'v'})/u'_{\text{rms}}v'_{\text{rms}}$ the flow developing section and 35% in the test section of the velocity fluctuations u' and v' , is a (blue square), biofilm (black asterisk). measure of the efficiency of wall-normal motion in transporting streamwise momentum (Figure 13A). The results indicate that at both Re , the coefficient has a nearly constant value of ~ 0.5 for $0 \lesssim y/d \lesssim 0.6$, and a peak at $y/d \approx -0.1$. The value of the peak decreases with porosity and is nearly flat for both the biofilm average and the non-biofilm reduced-porosity bed (nBF-45-35%).

3.3 Quadrant Analysis

Quadrant analysis of the instantaneous velocity fields was performed to gain further insight into trends observed in the RSS (Wallace 2016). In this approach, $u'v'$ is classified into four categories, termed quadrants (Q), based on the sign of u' and v' : Q1 ($u' > 0$, $v' > 0$), Q2 ($u' < 0$, $v' > 0$), Q3 ($u' < 0$, $v' < 0$), and Q4 ($u' > 0$, $v' < 0$), where Q2 and Q4 events are referred to as ejections and sweeps, respectively, and Q1 and Q3 events are called outward and inward interactions. The hyperbolic hole size method of Lu and Willmarth (1973), with a hole size of $\eta = 4$ has been applied herein. Thus, only the intense Reynolds-stress-producing events above the $\eta = 4$ threshold have been considered. In this configuration, contributions from Q2 and Q4 were stronger than that of Q1 and Q3 by a factor of >10 , and thus only data for Q2 and Q4 are considered further. For the flow with biofilm, only one of the three separate datasets is considered herein (BF1).

The contributions from Q2 and Q4 to the Reynolds shear stress, non-dimensionalized with $(u_\tau^p)^2$ and in absolute units, are presented in Figure 14A and B, respectively. For the biofilm bed, the Q2 and Q4 contributions shift in a +y-direction compared to the non-biofilm datasets. The crossover between Q2 and Q4 contributions for the two non-biofilm beds (nBF-45% and nBF-45-35%) occurred at $y/d \approx 0$, while for the biofilm bed (BF1) the crossover occurred at $y/d \approx 0.2$. Similarly, while Q4 contributions had a maximum near $y/d \approx -0.1$ for the non-biofilm beds, the peak for BF1 occurred closer to the cylinder crests at $y/d \approx -0.05$. The peak for contributions from Q2 events occurred at $y/d \approx 0.4$ for the nBF-45% dataset and at $y/d \approx 0.5$ for nBF-45-35% and BF1 datasets. In absolute units, the Q4 contributions (Figure 14B) for the two non-biofilm beds were in relatively close agreement, while BF1 had a wider and taller peak compared to the two non-biofilm datasets. Additionally, the Q2 contributions for flow over the biofilm bed were stronger than both non-biofilm beds for $0.25 \lesssim y/d \lesssim 1$. Thus, for nearly all vertical positions, the intense Q2 and Q4 Reynolds shear stresses for BF1 were stronger than the two nBF datasets, except for $0 \lesssim y/d \lesssim 0.2$ where nBF-45% had a higher Q2 Reynolds shear stress contribution.



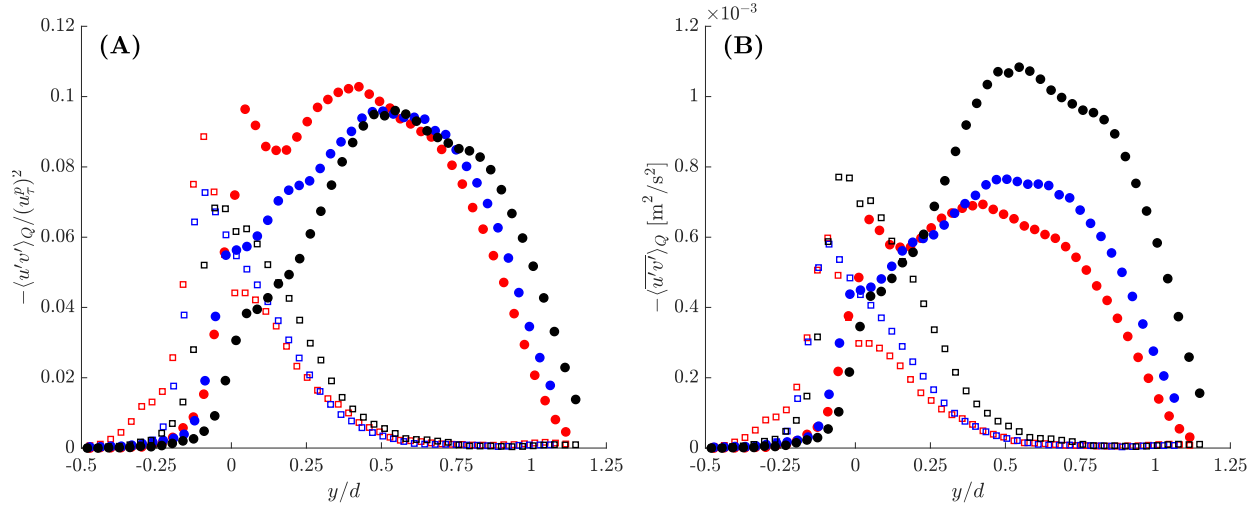


Figure 14. Quadrant analysis showing the distribution of high-intensity Q2 and Q4 (Hole size, $\eta = 4$) for $f = 30$ Hz ($Re = 11150 \pm 700$). (A) Normalized with $(u_{\tau}^p)^2$, and (B) in absolute units.

4 Discussion

In comparing flow with and without biofilm at constant pump frequency, f (and hence flow discharge), the present results demonstrate that flow over a bed with biofilm had slightly higher maximum double-averaged streamwise velocity (U_{max}) above the bed compared to the no biofilm case. This increase in U_{max} was concomitant with an increase in bulk velocity, U_b , resulting in highly similar velocity profiles for the biofilm and non-biofilm beds (Figures 7A and 9A). The increase in U_b in the presence of biofilm is expected based on the reduction in bed porosity while the total volumetric flow rate, Q , measured by the flow meter, remained nearly constant.

The double-averaged wall-normal velocity, $\langle \bar{v} \rangle$, in all cases, was very close to zero, for $y/d \gtrsim 0.25$, indicating a purely horizontal flow, as would be expected. In addition, the before and after detachment (BF–BD and BF–AD) profiles were qualitatively similar. In all cases of flow over the biofilm bed and the non-biofilm reduced porosity bed (nBF-45-35%), the profile showed a weak upward velocity for $-0.5 \lesssim y/d \lesssim -0.1$ (Figures 7B and 9B). The occurrence of the upward motion was likely due to the experimental configuration with a transition in bed porosity before the measurement module, as explained in §2.1. This apparent deflection of flow from the permeable bed to the free flow was observed in all cases except for the nBF-45% case where the entire bed had constant porosity.

The logarithmic fit to the streamwise velocity profile, Eq. (8), yielded dimensionless equivalent roughness height (k_s^+) and zero displacement height (y_0^+) that are smaller for the biofilm after detachment (BF–AD) compared to the before detachment (BF–BD) case, at constant pump frequency. In a similar manner, comparing flow with and without biofilm (Figure 10), revealed a consistent increase in k_s^+ and y_0^+ in the presence of biofilm. Moreover, for all flow conditions y_0^+ increased with Re_K consistent with previous results by Suga et al. (2010) and Fang et al. (2018). The von Kármán constant for the logarithmic fit, κ , also decreased with increasing Re_K with and without biofilm, consistent with previous studies (Fang et al. 2018; Nezu 2005; Suga et al. 2010). However, it should be highlighted that there are a few exceptions to this trend. Specifically,

when comparing the flow without biofilm over the reduced porosity bed (nBF-45-35%) and the reference flow (nBF-45%) at constant pump frequency, y_0^+ and k_s^+ increased and κ decreased with decreasing bed permeability. Although we cannot determine the exact reason for this behavior, we speculate this effect is due to the developing nature of flow in the nBF-45-35% case.

The biofilm coverage depicted in Figure 6 shows a gradual decrease in biofilm coverage due to detachment from flow shear. Unlike the velocity profiles that were unaffected significantly by biofilm detachment, the Reynolds stresses experienced a more pronounced impact. Taking together the results from flow over the biofilm bed before and after detachment (Figure 8) as well as with and without biofilm (Figure 11), it is observed that at constant pump frequency, the Reynolds stresses, scaled with $(u_\tau^p)^2$ for $0.4 \lesssim y/d \lesssim 1$ (outer layer). Close to the bed surface $0 \lesssim y/d \lesssim 0.4$ (inner layer) this scaling is absent, where in all cases, the dimensionless Reynolds stresses, were dampened in the presence of biofilm. Moreover, for flow over the biofilm bed, as well as the reduced porosity bed (nBF-45-35%), the maximum Reynolds shear stress (Figure 8C) occurred higher above the cylinder crest at $y/d \approx 0.1$, compared to $y/d \approx 0$ for the reference non-biofilm bed. This trend was consistent with the effect of decreased bed porosity observed in previous studies (Breugem et al., 2006).

The quadrant analysis of Reynolds shear stress contributions with a hole size of $\eta = 4$ showed that for all bed configurations, sweep (Q4) events were strongest near the bed, while ejection events (Q2) were dominant away from the bed surface, for all flow configurations (Figure 14). This was expected from previous studies of flow over permeable beds (Suga et al. 2011). Quadrant analysis revealed that the decrease in dimensionless Reynolds shear stress in the inner layer, in the presence of biofilm, stems primarily from a reduction in Q2 contributions for $0 \lesssim y/d \lesssim 0.5$, offset by a modest increase in Q4 contributions.

All form-induced stresses were nearly zero and negligible above the cylinder crests for all datasets. This is in contrast to the findings from past studies (Fang et al. 2018; Manes et al. 2009; Pokrajac et al. 2007), and is likely due to the shallow submergence ratio of the roughness elements to the flow depth. To facilitate comparison with studies in open channels, the effective flow depth can be taken as y_{max} (i.e. distance of maximum $\langle \bar{u} \rangle$ from the cylinder crest). Hence, the d/y_{max} ratio in the present study is ~ 1 , whereas the flow depth to roughness height ratio was 3.5 in Fang et al. (2018), 6–15 in Pokrajac et al. (2007) and 1.67–3.5 in Manes et al. (2009). Below the cylinder crests, for $-0.5 \lesssim y/d \lesssim 0$, the form-induced stress terms were significant and, in some instances, greater than their Reynolds stress counterparts. The biofilm datasets had a wide range of variation that can translate to increases or decreases in form-induced stresses relative to the non-biofilm beds. This illustrates the fact that compared to Reynolds stresses, form-induced stresses are more sensitive to inter-dataset variations.

The peak value of the correlation coefficient (Figure 13) of ~ 0.5 near the cylinder crest was similar to that of flow observed at the top of a vegetation canopy (Finnigan, 2000). Notably, while there is not a universal profile for correlation coefficient for different vegetation canopies, the value at the canopy top from studies in different configuration all fall within the range 0.4–0.5. Moreover, the decreased correlation coefficient for flow over a biofilm bed as compared to

the case without biofilm was similar to the effect expected with reduced bed porosity (Breugem et al., 2006).

In assessing the impact of biofilm presence on flow over a permeable bed with a given geometry, at least two competing effects may be considered: 1) reduced bed porosity concomitant with a likely reduction in bed permeability, and 2) increased roughness and change in geometry at the top of the cylinders. Reduced bed porosity/permeability has a damping effect on Reynolds stresses (Breugem et al., 2006; Suga et al., 2010) while increased roughness has the opposite effect. Studies of flow over smooth impermeable walls have shown that the equivalent roughness for biofilm is larger than its physical roughness, owing to its motion in the flow (Schultz et al., 2015). To test the impact of reduced bed porosity, but without any roughness effect, we used a permeable test module with reduced porosity (35% instead of 45%) but with the same roughness using the same arrangement of cylinders in the top layer (Figure 1G). Interestingly, at a constant pump frequency of $f = 30$ Hz ($Re = 11150 \pm 700$), the dimensionless Reynolds stress profiles (Figure 11) showed close agreement between the non-biofilm reduced porosity bed (nBF-45-35%) and the biofilm average, in contrast to trends at lower frequencies. This is, in part, due to the fact that at the highest tested flow rate herein, the biofilm coverage on cylinder crests was mostly detached, while some biofilm remained attached at lower pump frequencies (c.f. Figure 6). Unlike the Reynolds stresses, the form-induced stresses (Figure 12), which are dominant below the cylinder crests, showed significant differences between the non-biofilm reduced porosity bed (nBF-45-35%) and the biofilm beds.

An important point to note here is that comparison of different studies is not a straightforward task, primarily due to the unique nature of different experimental configurations in terms of bed configuration (porosity, grain size), and perhaps even more importantly, due to broad variations in biofilm coverage and method of growth. Very few studies have reported velocity measurements over *permeable* beds *with* biofilm. Our results indicate higher wall shear stress as a result of the presence of biofilm in flow over a permeable bed (Table 2). However, in open channel flow over rough *impermeable* beds with 20-mm tall hemispheres, Graba et al. (2010) showed that biofilm growth results in slightly lower wall shear stress. Nikora et al. (2002) used a nearly identical rough impermeable geometry as that used by Graba et al. (2010) and, instead, reported no change in wall shear stress. One major difference between the present study and those of Graba et al. (2010) and Nikora et al. (2002) is that the rough wall was impermeable in these previous studies, which is not representative of natural gravel-bed rivers. Another factor worthy of note is the extent of biofilm growth and coverage. In the study of Graba et al. (2010), the biofilm occupied the space between the hemispherical roughness elements (pebbles), whilst in Nikora et al. (2002) biofilm covered the entire bed as a thick mat, thus completely changing the nature of the roughness and the bed. However, in the current study the biofilm remained as a heterogenous film covering the cylinders but without connecting the adjacent cylinders (at least in the top row which was easily visible). Moreover, the increased wall-normal Reynolds normal stress in absolute units in the presence of biofilm reported herein are in contrast to results from Vignaga et al. (2013). This discrepancy can be attributed to the experimental configuration, as Vignaga et al. (2013) conducted their experiments with 20-mm-deep beds consisting of grains 1–2.2 mm in diameter, and with a free flow depth of 30–40 mm. Their observed decrease in wall-normal velocity fluctuations (no results on streamwise fluctuations or *RSS* were reported) can, in part, be attributed to the shallow depth of the bed relative to the free flow, as suggested by the

results of Kim et al. (2018). Moreover, the reduced velocity fluctuations reported by Vignaga et al. (2013), may be a result of biofilm smoothing the surface, similar to that observed by Graba et al. (2010) and Nikora et al. (2002) as the biofilm growth resulted in a sediment-biofilm composite material.

Figure 15 summarizes the key processes involved in flow over a permeable bed with biofilm as studied herein. The main question that we attempted to address was how the reduced bed porosity and change in roughness combine to modify flow.

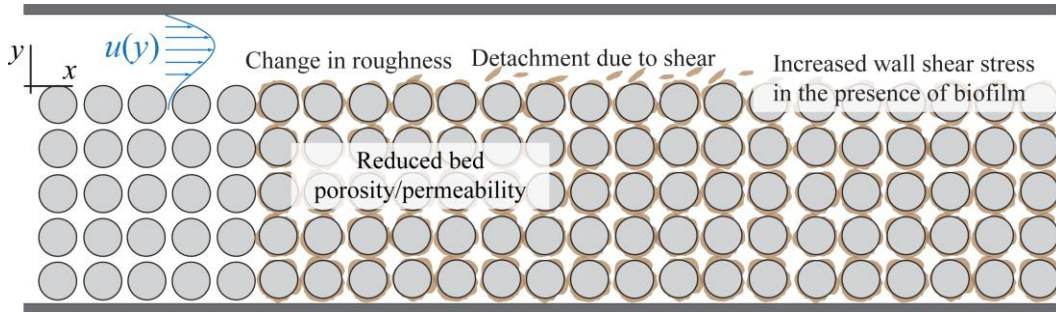


Figure 15. Processes involved in flow over a permeable bed with biofilm as investigated in the present work.

5 Limitations and Implications of the Flow Apparatus

The results of the present study are inevitably impacted by choices in the design of the experimental apparatus and protocol that could exert an influence but whose impact has not been studied herein. One such effect is the spanwise variations for the BF datasets. While the incoming flow conditions during biofilm development were maintained as uniform as possible in the spanwise direction, non-uniformity in biofilm growth and biomass accumulation in the spanwise direction could have occurred. Specifically, near the side walls, the distribution of biomass could be different from the mid-plane.

In addition, biofilm coverage in the flow channel was limited to a 0.30-m long portion (referred to as the *measurement module*) in the test section as biofilm was developed in a standalone recirculating reactor (c.f. §2.2). This was done primarily to avoid undesired biofilm growth on the glass window and in portions of the water channel with limited access for cleaning. As such, a transition in bed geometry occurred at the beginning of the test section meaning that the flow was likely not fully developed for the cases of flow with biofilm (BF datasets) and reduced-porosity-bed (nBF-45-35%). Despite this limitation, the experiments reported herein were not intended to provide a comprehensive set of universal results that can be used for comparison with other studies or natural gravel-bed rivers. Rather, given the scarcity of data on this topic, our goal was to investigate the first-order effects of biofilm presence on a permeable bed. As such, while not universal, the results presented herein provide a robust comparative study between fundamentally different biofilm coverage configurations under the same controlled conditions. Indeed, further studies are required to explore the flow dynamics and biofilm interactions over a much broader set of conditions, but that is outside the focus of this contribution.

It is also worthy to consider whether the method of biofilm development (i.e. in a separate reactor at low Re and shear) could influence the results. In particular, the shear stress experienced by the biofilm was significantly higher during the flow experiments than during the growth stage. Vignaga et al. (2013) used a similar approach for part of their experiments to test the influence of biofilm at different stages of development. In other studies, however, the biofilm development and growth were conducted under the same flow conditions (i.e. Re and shear) as the flow experiments. The significance of this difference could be increased attachment and cohesive strength of biofilms developed under high shear (Stoodley et al., 2002), resulting in a denser biofilm compared to the present study. As a result, in the present study, progressive biofilm detachment occurred as the flow rate was increased. This particular scenario may be similar to that which occurs during flood events in natural channels, where biofilms experience abrupt increases and decreases in flow-induced shear during unsteady flow conditions.

Finally, the flow facility used in the present study consisted of a closed channel with no free surface, whereas in past studies, (e.g. Graba et al. 2010; Nikora et al. 2002; Vignaga et al. 2013) an open channel was employed. A closed channel was used herein with a smooth impermeable top wall to permit optical access and better control over boundary conditions. Although the top smooth impermeable wall can dampen pressure fluctuations compared to the case of an open channel flow, turbulence effects are still dominated by the rough permeable bottom wall. s such, despite these differences, the results presented herein provide insight into the effect of biofilm on flow over a permeable bed. In this regard, we expect the trends observed in Reynolds stresses in the presence of biofilm, as well as before and after biofilm detachment, to be applicable (at least qualitatively) to open channel flows with similar Re_K and Re_T^p .

6 Summary and Conclusions

The effect of biofilms on flow structure over a permeable bed was quantified using PIV measurements in a closed-top recirculating channel flow. In order to account for the variability in biofilm growth, three separate biofilm batches were developed and tested. One of the ways that biofilm presence can affect flow over a permeable bed is through a reduction in bed porosity by biomass occupying the pore spaces. This effect was investigated by testing flow over a reduced-porosity bed without biofilm. The results showed that, while certain aspects of the effect of biofilm presence on flow can be replicated with reduced bed porosity without biofilm, the effect of biofilm is highly complicated and full understanding of the two-way interaction between flow and biofilms requires further investigation. The following main conclusions can be drawn from the present study:

1. The wall shear stress and friction velocity, obtained from the total shear stress, consistently increased in the presence of biofilm, and subsequently decreased as a result of biofilm detachment, when compared at the same pump frequency (flow discharge).
2. At the same flow discharge, the equivalent roughness height, k_s^+ , and zero displacement height, y_0^+ , were lower for the biofilm after detachment (BF–AD) compared to before detachment (BF–BD). Additionally, k_s^+ and y_0^+ were higher in the presence of biofilm compared to the no biofilm datasets.
3. In all flow configurations studied herein (with and without biofilm) at the same flow discharge, the individual components of Reynolds stresses normalized with $(u_\tau^p)^2$ collapsed for $\sim 0.4 < y/d < 1$ (outer layer), while the dimensionless Reynolds stresses decreased in the presence of biofilm for $0 \lesssim y/d \lesssim 0.25$ (inner layer).

4. Quadrant analysis (hole size, $\eta = 4$) suggests that the reduction in dimensionless Reynolds shear stresses in the inner layer in the presence of biofilm is primarily due to a reduction in strong Q2 contributions.

Turbulence plays a major role in mass and momentum exchange across the bed interface between the free and subsurface flow in a wide range of geophysical flows. Our results suggest that models for flow and transport over such permeable media in aquatic environments cannot neglect the role of biofilms in modifying turbulence. In light of the observations reported herein, the following are important areas that were not considered in the present study, but constitute profitable topics for future investigations:

1. In-situ imaging and quantification of biofilm morphology can help elucidate the two-way coupling between turbulence and biofilm growth/detachment. Distribution of biomass in the spanwise and wall-normal directions of the bed may create non-negligible three-dimensional effects in the flow.
2. The dynamic interactions between free and subsurface flow in the presence of biofilm is worthy of further investigation. However, non-intrusive measurement and optical access are expected to be major obstacles to investigating flow inside the bed.

Acknowledgment

We thank the UK Natural Environment Research Council for funding this work (NE/K012819/1), and Monica Ochoa for her help in running and maintaining the biofilm reactor. We are also thankful to the anonymous reviewers whose comments helped improve the paper greatly. All experiments were undertaken in the Department of Aerospace and Mechanical Engineering at the University of Notre Dame. Data used in the manuscript is available for download at <https://doi.org/10.3886/E118207V1>.

References

- Aubeneau, A. F., Brittany Hanrahan, Diogo Bolster, and Jennifer Tank. 2016. "Biofilm Growth in Gravel Bed Streams Controls Solute Residence Time Distributions." *Journal of Geophysical Research: Biogeosciences* 121(7):1840–50.
- Battin, Tom J., Louis A. Kaplan, J. Denis Newbold, and Claude M. E. Hansen. 2003. "Contributions of Microbial Biofilms to Ecosystem Processes in Stream Mesocosms." *Nature* 426(6965):439–42.
- Battin, Tom J., William T. Sloan, Staffan Kjelleberg, Holger Daims, Ian M. Head, Tom P. Curtis, and Leo Eberl. 2007. "Microbial Landscapes: New Paths to Biofilm Research." *Nature Reviews. Microbiology* 5(1):76–81.
- Blois, G., G. H. Sambrook Smith, J. L. Best, R. J. Hardy, and J. R. Lead. 2011. "Quantifying the Dynamics of Flow within a Permeable Bed Using Time-Resolved Endoscopic Particle Imaging Velocimetry (EPIV)." *Experiments in Fluids* 53(1):51–76.
- Blois, G., G. H. Sambrook Smith, J. L. Best, R. J. Hardy, and J. R. Lead. 2012. "Quantifying the Dynamics of Flow within a Permeable Bed Using Time-Resolved Endoscopic Particle Imaging Velocimetry (EPIV)." *Experiments in Fluids* 53(1):51–76.

- 756 Blois, Gianluca, James L. Best, Gregory H. Sambrook Smith, and Richard J. Hardy. 2014.
757 “Effect of Bed Permeability and Hyporheic Flow on Turbulent Flow over Bed Forms.”
758 *Geophysical Research Letters* 41(18):6435–42.
- 759 Boano, F., J. W. Harvey, a. Marion, a. I. Packman, R. Revelli, L. Ridolfi, and a. Wörman. 2014.
760 “Hyporheic Flow and Transport Processes: Mechanisms, Models, and Biogeochemical
761 Implications.” *Reviews of Geophysics* 1–77.
- 762 Breugem, W. P. and B. J. Boersma. 2005. “Direct Numerical Simulations of Turbulent Flow
763 over a Permeable Wall Using a Direct and a Continuum Approach.” *Physics of Fluids*
764 17(2):025103.
- 765 Breugem, Wim-Paul, B. J. Boersma, and R. E. Uittenbogaard. 2006. “The Influence of Wall
766 Permeability on Turbulent Channel Flow.” *Journal of Fluid Mechanics* 562:35.
- 767 Cardenas, M. Bayani. 2015. “Hyporheic Zone Hydrologic Science: A Historical Account of Its
768 Emergence and a Prospectus.” *Water Resources Research* n/a-n/a.
- 769 Carrel, M., V. L. Morales, M. Dentz, N. Derlon, E. Morgenroth, and M. Holzner. 2018. “Pore-
770 Scale Hydrodynamics in a Progressively Bioclogged Three-Dimensional Porous Medium:
771 3-D Particle Tracking Experiments and Stochastic Transport Modeling.” *Water Resources*
772 *Research* 1–16.
- 773 Dzubakova, Katharine, Hannes Peter, Enrico Bertuzzo, Carmelo Juez, Mário J. Franca, Andrea
774 Rinaldo, and Tom J. Battin. 2018. “Environmental Heterogeneity Promotes Spatial
775 Resilience of Phototrophic Biofilms in Streambeds.” *Biology Letters* 14(10):0–3.
- 776 Fang, Hongwei, Xu Han, Guojian He, and Subhasish Dey. 2018. “Influence of Permeable Beds
777 on Hydraulically Macro-Rough Flow.” *Journal of Fluid Mechanics* 847:552–90.
- 778 Finnigan, John. 2000. “Turbulence in Plant Canopies.” *Annual Review of Fluid Mechanics*
779 32(1):519–71.
- 780 Frostick, Lynne E. and I. Nicholas McCave. 1979. “Seasonal Shifts of Sediment within an
781 Estuary Mediated by Algal Growth.” *Estuarine and Coastal Marine Science* 9(5):569–76.
- 782 Graba, Myriam, Frédéric Y. Moulin, Stéphanie Boulêtreau, Frédéric Garabétian, Ahmed Kettab,
783 Olivier Eiff, José Miguel Sánchez-Pérez, and Sabine Sauvage. 2010. “Effect of Near-Bed
784 Turbulence on Chronic Detachment of Epilithic Biofilm: Experimental and Modeling
785 Approaches.” *Water Resources Research* 46(11):n/a-n/a.
- 786 Graba, Myriam, Sabine Sauvage, Frédéric Y. Moulin, Gemma Urrea, Sergi Sabater, and José
787 Miguel Sanchez-Pérez. 2013. “Interaction between Local Hydrodynamics and Algal
788 Community in Epilithic Biofilm.” *Water Research* 47(7):2153–63.
- 789 Grant, Stanley B., Jesus D. Gomez-Velez, and Marco Ghisalberti. 2018. “Modeling the Effects
790 of Turbulence on Hyporheic Exchange and Local-to-Global Nutrient Processing in
791 Streams.” *Water Resources Research* (1):5883–89.

- 792 Kim, Taehoon, Gianluca Blois, James L. Best, and Kenneth T. Christensen. 2018. “Experimental
793 Study of Turbulent Flow over and within Cubically Packed Walls of Spheres: Effects of
794 Topography, Permeability and Wall Thickness.” *International Journal of Heat and Fluid*
795 *Flow* 73(May):16–29.
- 796 Kim, Taehoon, Gianluca Blois, James L. Best, and Kenneth T. Christensen. 2019. “PIV
797 Measurements of Turbulent Flow Overlying Large, Cubic- and Hexagonally-Packed
798 Hemisphere Arrays.” *Journal of Hydraulic Research* 1686.
- 799 Kim, Taehoon, Gianluca Blois, James L. Best, and Kenneth T. Christensen. 2020. “Experimental
800 Evidence of Amplitude Modulation in Permeable-Wall Turbulence.” *Journal of Fluid*
801 *Mechanics*.
- 802 Lichtman, Ian D., Jaco H. Baas, Laurent O. Amoudry, Peter D. Thorne, Jonathan Malarkey, Julie
803 A. Hope, Jeffrey Peakall, David M. Paterson, Sarah J. Bass, Richard D. Cooke, Andrew J.
804 Manning, Alan G. Davies, Daniel R. Parsons, and Leiping Ye. 2018. “Bedform Migration in
805 a Mixed Sand and Cohesive Clay Intertidal Environment and Implications for Bed Material
806 Transport Predictions.” *Geomorphology* 315:17–32.
- 807 Lu, S. S. and W. W. Willmarth. 1973. “Measurements of the Structure of the Reynolds Stress in
808 a Turbulent Boundary Layer.” *Journal of Fluid Mechanics* 60(03):481.
- 809 Malarkey, Jonathan, Jaco H. Baas, Julie A. Hope, Rebecca J. Aspden, Daniel R. Parsons, Jeff
810 Peakall, David M. Paterson, Robert J. Schindler, Leiping Ye, Ian D. Lichtman, Sarah J.
811 Bass, Alan G. Davies, Andrew J. Manning, and Peter D. Thorne. 2015. “The Pervasive Role
812 of Biological Cohesion in Bedform Development.” *Nature Communications* 6:1–6.
- 813 Manes, C., D. Poggi, and L. Ridolfi. 2011. “Turbulent Boundary Layers over Permeable Walls:
814 Scaling and near-Wall Structure.” *Journal of Fluid Mechanics* 687:141–70.
- 815 Manes, C., D. Pokrajac, V. I. Nikora, L. Ridolfi, and D. Poggi. 2011. “Turbulent Friction in
816 Flows over Permeable Walls.” *Geophysical Research Letters* 38(3):n/a–n/a.
- 817 Manes, Costantino, Dubravka Pokrajac, Ian McEwan, and Vladimir Nikora. 2009. “Turbulence
818 Structure of Open Channel Flows over Permeable and Impermeable Beds: A Comparative
819 Study.” *Physics of Fluids* 21(12):1–12.
- 820 Nakayama, A., F. Kuwahara, and Y. Sano. 2007. “Concept of Equivalent Diameter for Heat and
821 Fluid Flow in Porous Media.” *AIChE Journal* 53(3):732–36.
- 822 Nezu, Iehisa. 2005. “Open-Channel Flow Turbulence and Its Research Prospect in the 21st
823 Century.” *Journal of Hydraulic Engineering* 131(4):229–46.
- 824 Nikora, V. I., D. G. Goring, and B. J. F. Biggs. 2002. “Some Observations of the Effects of
825 Micro-Organisms Growing on the Bed of an Open Channel on the Turbulence Properties.”
826 *Journal of Fluid Mechanics* 450:317–41.
- 827 Nikora, Vladimir, Derek Goring, Ian McEwan, and George Griffiths. 2001. “Spatially Averaged

- 828 Open-Channel Flow over Rough Bed.” *Journal of Hydraulic Engineering* 127(2):123–33.
- 829 Packman, Aaron I. and K. E. Bencala. 2000. “Modeling Surface-Subsurface Hydrological
830 Interactions.” Pp. 45–80 in *Streams and Ground Waters*.
- 831 Parsons, Daniel R., Robert J. Schindler, Julie A. Hope, Jonathan Malarkey, Jaco H. Baas, Jeffrey
832 Peakall, Andrew J. Manning, Leiping Ye, Steve Simmons, David M. Paterson, Rebecca J.
833 Aspden, Sarah J. Bass, Alan G. Davies, Ian D. Lichtman, and Peter D. Thorne. 2016. “The
834 Role of Biophysical Cohesion on Subaqueous Bed Form Size.” *Geophysical Research*
835 *Letters* 43(4):1566–73.
- 836 Pokrajac, Dubravka, Lorna Jane Campbell, Vladimir Nikora, Costantino Manes, and Ian
837 McEwan. 2007. “Quadrant Analysis of Persistent Spatial Velocity Perturbations over
838 Square-Bar Roughness.” *Experiments in Fluids* 42(3):413–23.
- 839 Pokrajac, Dubravka and Costantino Manes. 2009. “Velocity Measurements of a Free-Surface
840 Turbulent Flow Penetrating a Porous Medium Composed of Uniform-Size Spheres.”
841 *Transport in Porous Media* 78(3):367–83.
- 842 Roche, K. R., G. Blois, J. L. Best, K. T. Christensen, A. F. Aubeneau, and A. I. Packman. 2018.
843 “Turbulence Links Momentum and Solute Exchange in Coarse-Grained Streambeds.”
844 *Water Resources Research* 54(5):3225–42.
- 845 Roche, K. R., J. D. Drummond, F. Boano, A. I. Packman, T. J. Battin, and W. R. Hunter. 2017.
846 “Benthic Biofilm Controls on Fine Particle Dynamics in Streams.” *Water Resources*
847 *Research* 53(1):222–36.
- 848 Rosti, Marco E., Luca Cortelezzi, and Maurizio Quadrio. 2015. “Direct Numerical Simulation of
849 Turbulent Channel Flow over Porous Walls.” *Journal of Fluid Mechanics* 784(2015):396–
850 442.
- 851 Schultz, M. P., J. M. Walker, C. N. Steppe, K. A. Flack, J. M. Walker, C. N. Steppe, and K. A.
852 Flack Impact. 2015. “Impact of Diatomaceous Biofilms on the Frictional Drag of Fouling-
853 Release Coatings.” *Biofouling* 31(9–10):759–73.
- 854 Sinha, Sumit, Richard J. Hardy, Gianluca Blois, James L. Best, and Gregory H. Sambrook
855 Smith. 2017. “A Numerical Investigation into the Importance of Bed Permeability on
856 Determining Flow Structures over River Dunes.” *Water Resources Research* 53(4):3067–
857 86.
- 858 Sternecker, Katharina, Romy Wild, and Juergen Geist. 2013. “Effects of Substratum Restoration
859 on Salmonid Habitat Quality in a Subalpine Stream.” *Environmental Biology of Fishes*
860 96(12):1341–51.
- 861 Stoesser, Thorsten and Wolfgang Rodi. 2007. “Large Eddy Simulation of Open-Channel Flow
862 Over Spheres.” Pp. 321–30 in *High Performance Computing in Science and*
863 *Engineering’06*. Springer Berlin Heidelberg.

- 864 Stoodley, P., R. Cargo, C. J. Rupp, S. Wilson, and I. Klapper. 2002. "Biofilm Material Properties
865 as Related to Shear-Induced Deformation and Detachment Phenomena." *Journal of*
866 *Industrial Microbiology & Biotechnology* 29(6):361–67.
- 867 Suga, K., Y. Matsumura, Y. Ashitaka, S. Tominaga, and M. Kaneda. 2010. "Effects of Wall
868 Permeability on Turbulence." *International Journal of Heat and Fluid Flow* 31(6):974–84.
- 869 Suga, K., M. Mori, and M. Kaneda. 2011. "Vortex Structure of Turbulence over Permeable
870 Walls." *International Journal of Heat and Fluid Flow* 32(3):586–95.
- 871 Suga, Kazuhiko, Yuka Nakagawa, and Masayuki Kaneda. 2017. "Spanwise Turbulence Structure
872 over Permeable Walls." *J. Fluid Mech* 822:186–201.
- 873 Sutherland, T. F., C. L. Amos, and J. Grant. 1998. "The Effect of Buoyant Biofilms on the
874 Erodibility of Sublittoral Sediments of a Temperate Microtidal Estuary." *Limnology and*
875 *Oceanography* 43(2):225–35.
- 876 Vignaga, Elisa, David M. Sloan, Xiaoyu Luo, Heather Haynes, Vernon R. Phoenix, and William
877 T. Sloan. 2013. "Erosion of Biofilm-Bound Fluvial Sediments." *Nature Geoscience*
878 6(9):770–74.
- 879 Walker, J. M., J. E. Sargison, and A. D. Henderson. 2013. "Turbulent Boundary-Layer Structure
880 of Flows over Freshwater Biofilms." *Experiments in Fluids* 54(12):1628.
- 881 Wallace, James M. 2016. "Quadrant Analysis in Turbulence Research: History and Evolution."
882 *Annual Review of Fluid Mechanics* 48(1):131–58.
- 883 Widdows, J., S. Brown, M. D. Brinsley, P. N. Salkeld, and M. Elliott. 2000. "Temporal Changes
884 in Intertidal Sediment Erodability: Influence of Biological and Climatic Factors."
885 *Continental Shelf Research* 20(10–11):1275–89.
- 886

Figure 1.

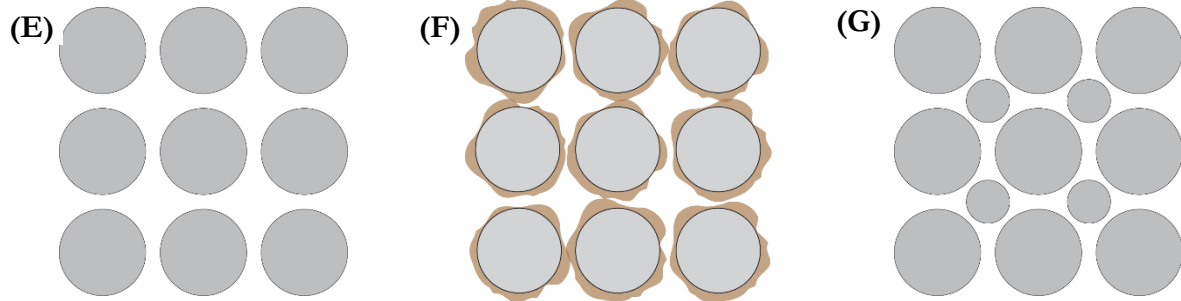
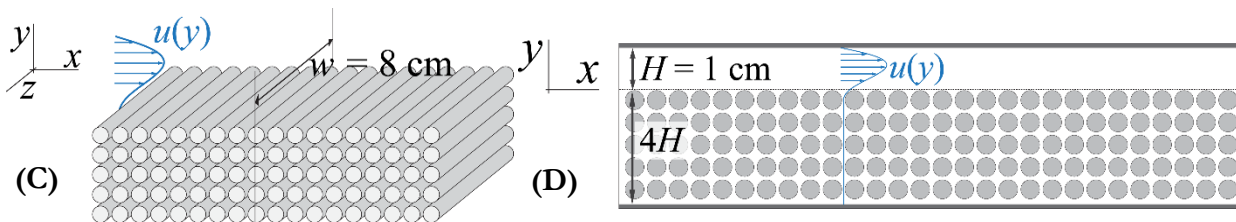
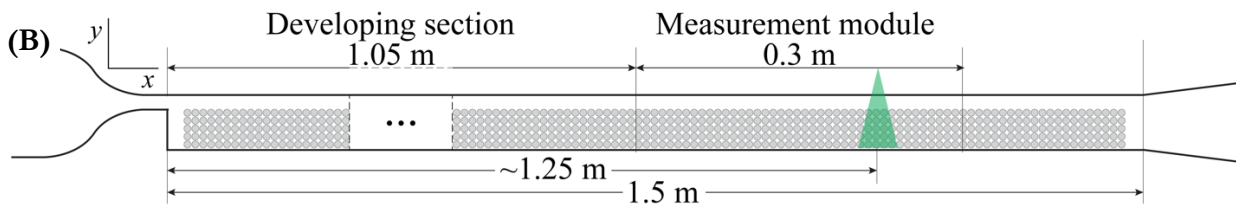
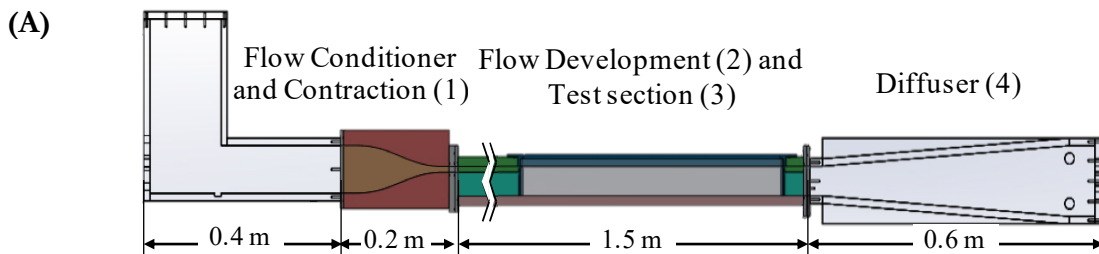
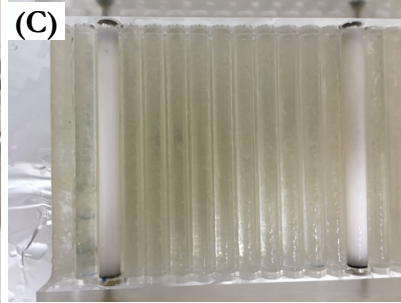
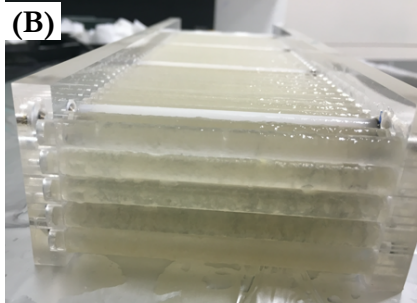
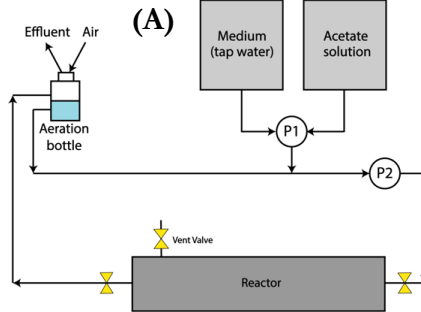


Figure 2.



P1: Influent peristaltic pump

P2: Recirculating gear pump

Figure 3.

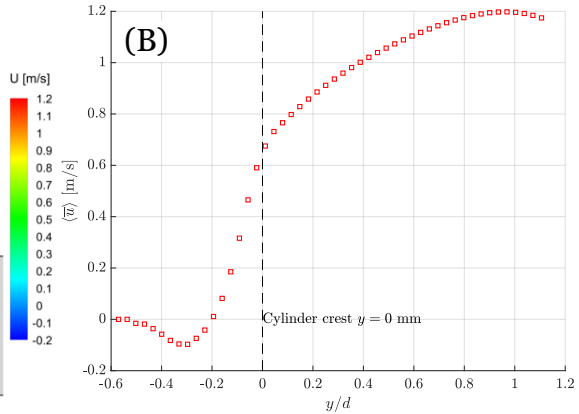
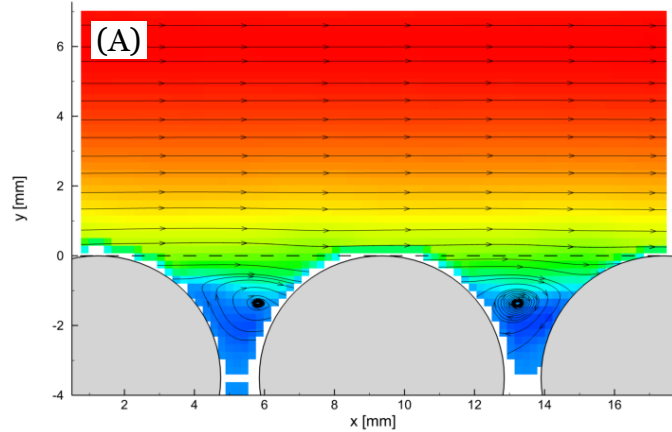


Figure 4.

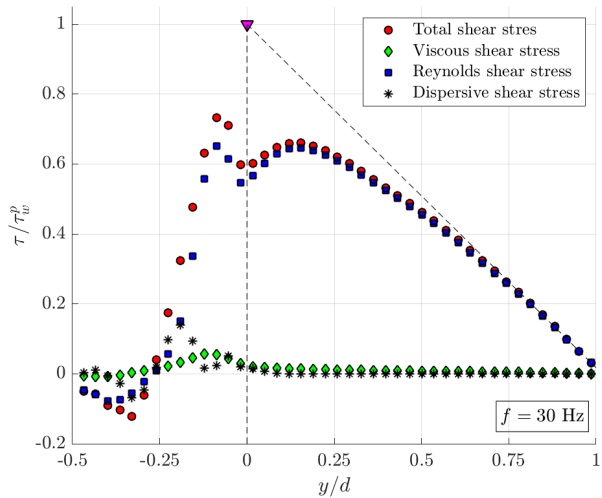


Figure 5.

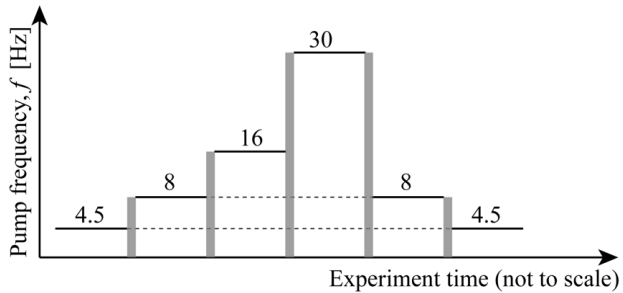


Figure 6.

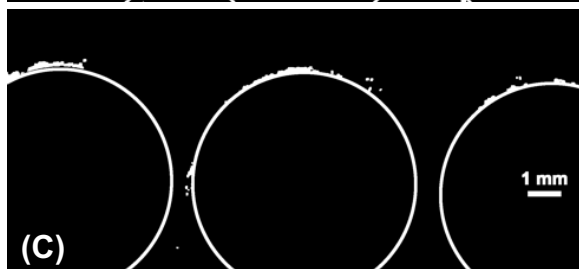
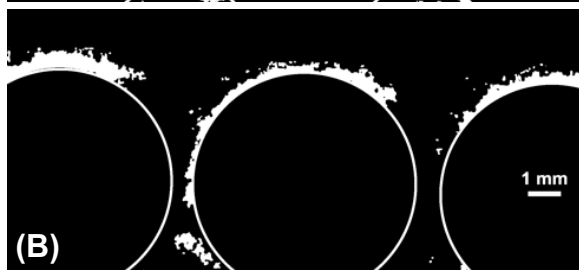


Figure 7.

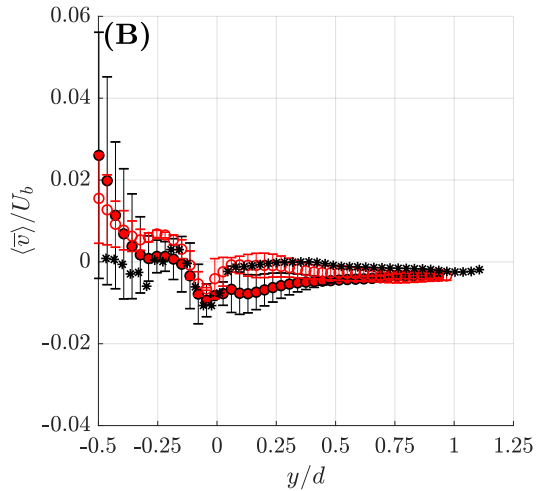
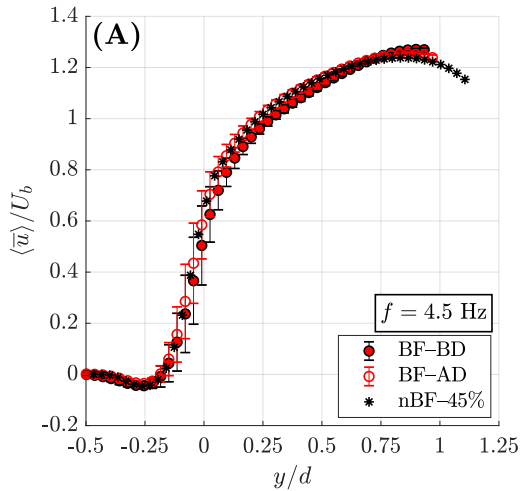


Figure 8.

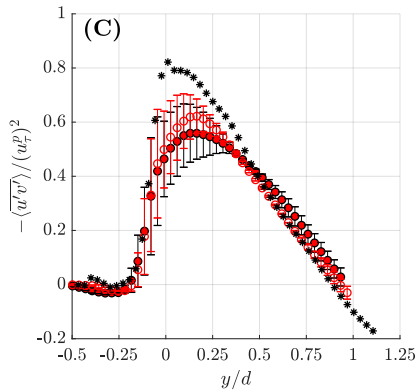
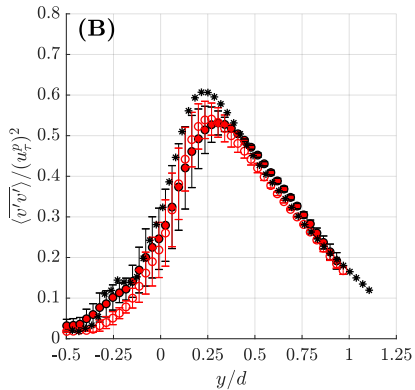
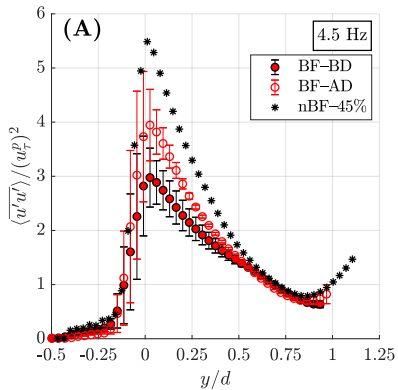


Figure 9.

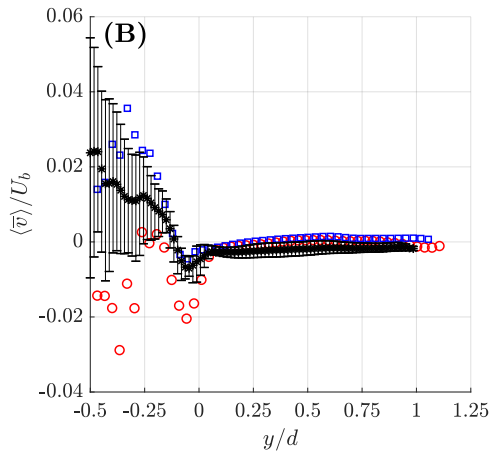
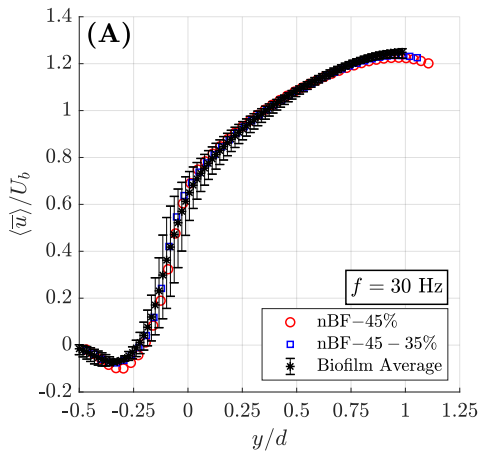


Figure 10.

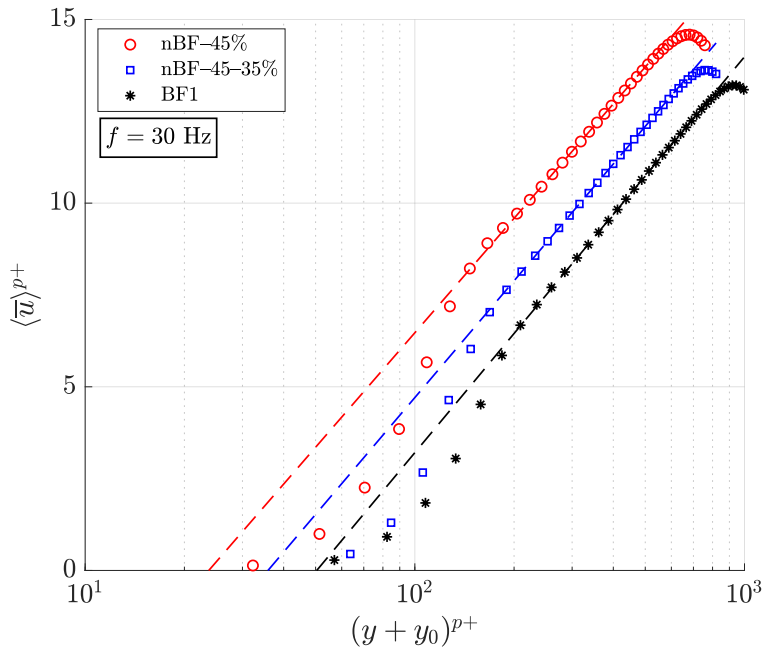


Figure 11.

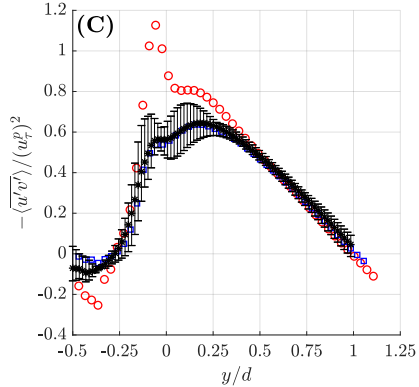
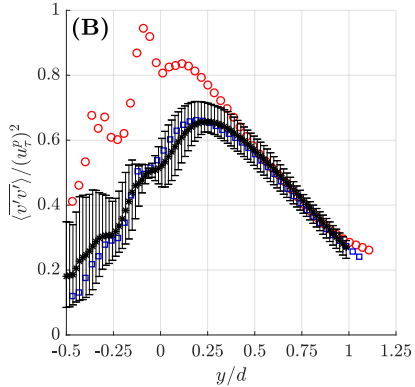
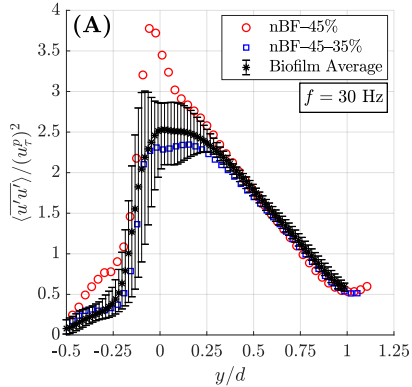


Figure 12.

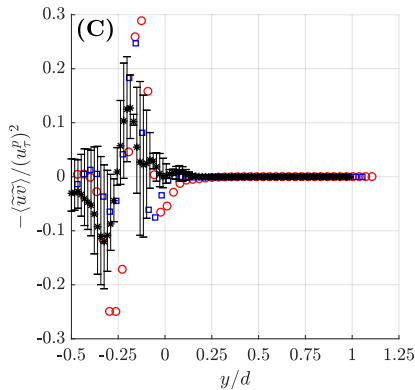
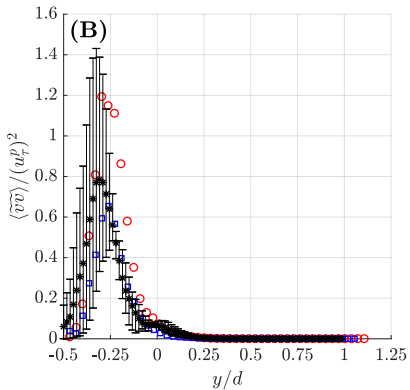
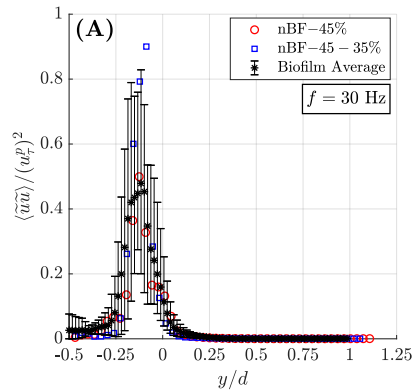


Figure 13.

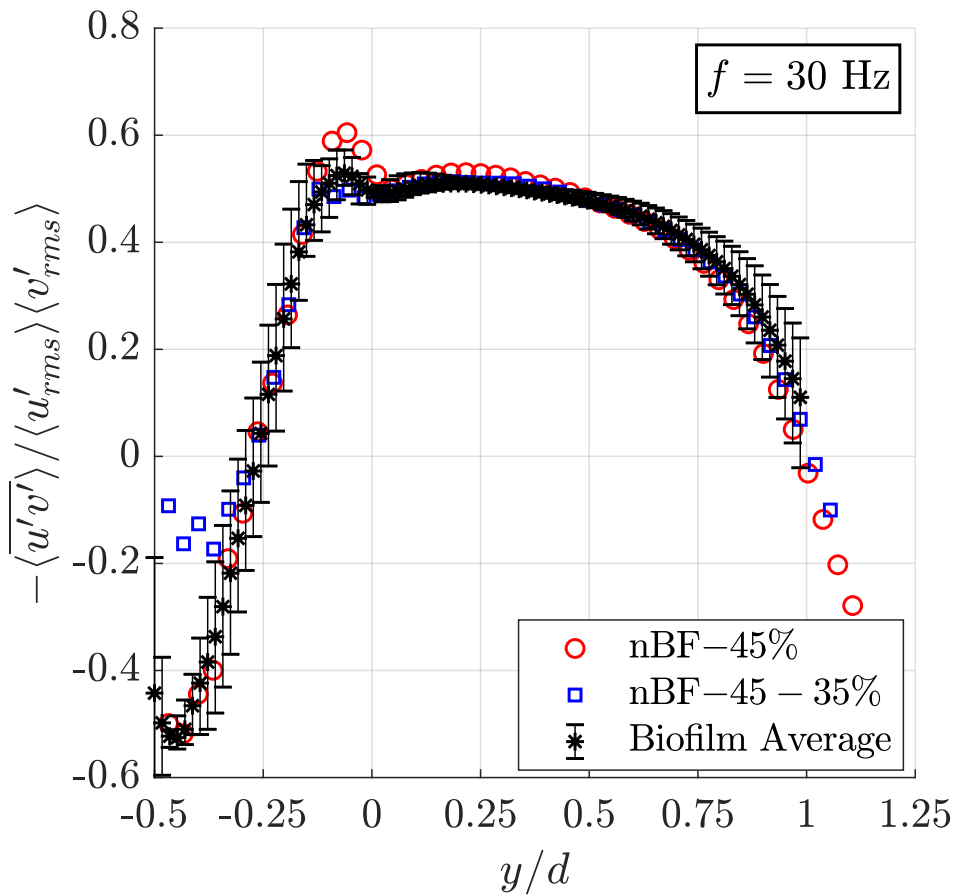


Figure 14.

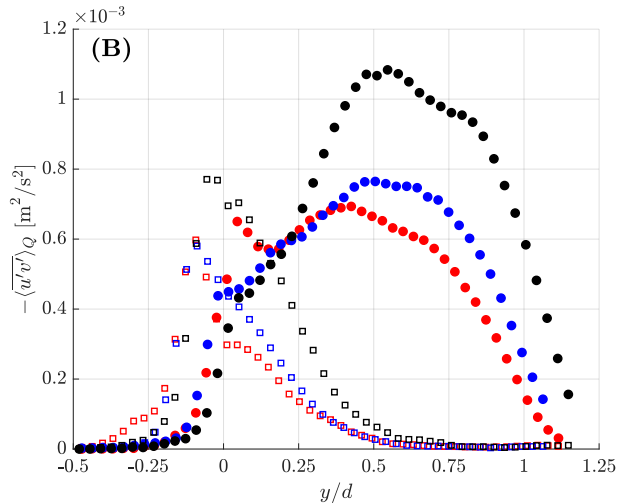
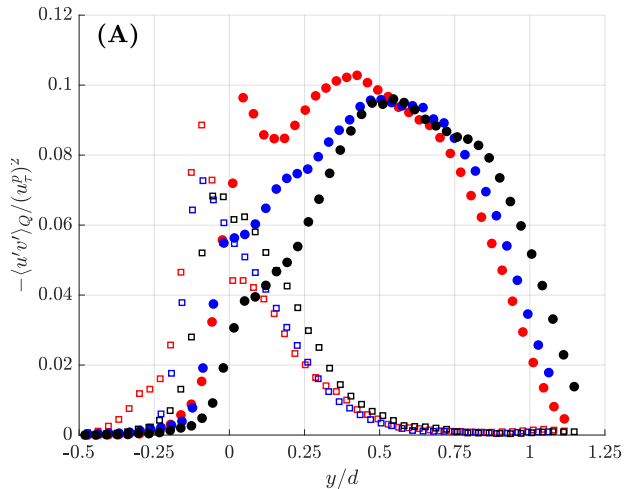
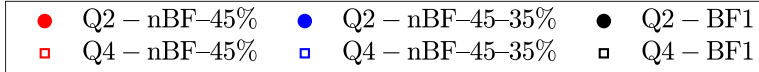


Figure 15.

